Galaxy Luminosity Function of the Coma Cluster from Deep u'-g'-r' Wendelstein Imaging Data

Raphael Zöller , ** Matthias Kluge , Ralf Bender , I Jan-Niklas Pippert , Benjamin Seidel , Claus Gössl , Ulrich Hopp , Hanna Kellermann , Christoph Ries, Arno Riffeser , Michael Schmidt, And Luis Thomas , Arno Riffeser , Michael Schmidt, And Luis Thomas ,

ABSTRACT

We derive the q' band galaxy luminosity function (GLF) of quenched red sequence in the Coma cluster from a deep-imaging survey with $\approx 1.5 \, \mathrm{deg^2}$ around the cluster center. The dataset comprises deep u'-, g'-, and r'-band data obtained with the Wendelstein Wide Field Imager on the 2.1 m Fraunhofer Wendelstein Telescope reaching median 3σ surface brightness limits in $10'' \times 10''$ boxes of $(30.0 \,\mathrm{u'}, \, 29.6 \,\mathrm{g'}, \, 28.7 \,\mathrm{r'}) \,\mathrm{mag \, arcsec^{-2}}$. We measure structural parameters across a large dynamic range in galaxy brightness ($-24.5\,g'\,\mathrm{mag} \lesssim M \lesssim -11.3\,g'\,\mathrm{mag}$), from the brightest cluster galaxy to low-luminosity dwarfs, including compact dwarf galaxies and ultra-diffuse galaxies. We automatically identify 5161 cluster member candidates based on their membership on the quiescent sequence in the u'-g' versus g'-r' color-color diagram and their red sequence membership. The structural parameters of bright galaxies are obtained via isophotal modeling, and fully automated parametric image fitting for faint ones. Injection-recovery tests and two identically analyzed reference fields provide statistical corrections for completeness and contamination, yielding a representative GLF that reliably probes the faint end and may serve as a benchmark for future studies. We report a best-fit double Schechter g' band GLF with a comparatively steep faint-end slope $\alpha_2 = -1.539^{+0.024}_{-0.024}$. We perform an applesto-apples comparison with the Coma counterpart in the SLOW simulations, finding overall agreement but a deficit of bright and an excess of dwarf galaxies in the simulation, despite its shallower faint-end slope, highlighting the need for true apples-to-apples comparisons that consider both normalization and slope for a consistent interpretation of the GLF.

Keywords: Galaxy Luminosity function(942) – Galaxy evolution(594) – Galaxy clusters(584) – Coma Cluster(270) – Abell clusters(9) – Galaxy photometry(611) – Galaxies(573) – Low surface brightness galaxies(940) – Dwarf galaxies(416) – Dwarf spheroidal galaxies(420) – Galaxy structure(622) – Extragalactic astronomy(506)

1. INTRODUCTION

The galaxy luminosity function (GLF) and the galaxy stellar mass function (GSMF) quantify the number density of galaxies per magnitude or mass interval, respectively, and are usually described by a Schechter (1976) function. They are important tools for understanding galaxy populations and galaxy evolution, as well as constraining cosmological models and dark matter models, by comparing observed GLFs (e.g., Binggeli et al. 1985; Efstathiou et al. 1988; Bernstein et al. 1995; Trentham 1998; Andreon & Cuillandre 2002; Mobasher et al. 2003; Blanton et al. 2005; Faber et al. 2007; Yamanoi et al.

2012; Ferrarese et al. 2016; Wright et al. 2017; Cuillandre et al. 2025) with the predicted GLFs from simulations (e.g., Kauffmann et al. 1993; Pillepich et al. 2018; Behroozi et al. 2019; Dolag et al. 2025). The tension between the predicted steep faint-end slope from first-generation cosmological simulations and observed flat slopes caused discussions about the "missing satellite problem" (e.g., Mateo 1998; Klypin et al. 1999; Moore et al. 1999). For observations, the major limitations are the corrections for completeness and contamination. For simulations, the treatment of baryonic physics is crucial as stellar winds and supernova feedback suppress the star formation in low mass galaxies, whereas AGN feedback suppresses the star formation in massive galaxies and hence affect the stellar mass – halo mass function,

¹ University Observatory, Faculty of Physics, Ludwig-Maximilians-Universität München, Scheinerstr. 1, 81679 Munich, Germany

² Max Planck Institute for Extraterrestrial Physics, Giessenbachstrasse, D-85748 Garching, Germany

^{*} rzoeller@mpe.mpg.de

leading to fewer dwarf galaxies, as well as explaining the decrease of luminous galaxies (e.g., Moster et al. 2010, 2013, 2018; Behroozi et al. 2019). Furthermore, the slope of the GLF and GSMF are powerful tools to probe dark matter models, i.e., cold dark matter predicts a high abundance of dwarf galaxies, whereas warm dark matter suppresses the formation of small halos (Menci et al. 2012; Bullock & Boylan-Kolchin 2017).

Recent deep imaging surveys have revealed a large number of low-surface brightness (LSB) galaxies such as ultra-diffuse galaxies (UDGs) (e.g., van Dokkum et al. 2015; Yagi et al. 2016; Venhola et al. 2019; Marleau et al. 2021; Zöller et al. 2024; Marleau et al. 2025a). In this study, we measure the GLF in the Coma cluster, including those most diffuse galaxies but also compact dwarf galaxies, and investigate whether they significantly contribute to the GLF, increasing its faint-end slope.

In this study, we focus on the GLF, but our Coma cluster galaxy sample also provides an excellent dataset to study the distribution of galaxies in various parameter spaces, which will be discussed in a complementary work in Zöller et al. (in prep.). Both our goals, determining the GLF and structural parameter correlation densities, require a correction for the selection function, i.e., correcting for contamination and completeness. Especially for dwarf galaxies, detecting and separating them from interloping galaxies to classify them as cluster members is a challenge. Many dwarf galaxy studies rely on visual inspection to identify them, either fully relying on visual inspection of images, or using a semi-automatic procedure, first automatically preselecting candidates, followed by a visual inspection (e.g., Binggeli et al. 1985; Müller et al. 2017; Wittmann et al. 2017; Venhola et al. 2017; Habas et al. 2020; Marleau et al. 2025a,b). Despite this giving relatively clean and complete dwarf galaxy samples, determining a selection function for visual inspection is problematic. In addition, upscaling to upcoming deep surveys such as Euclid (Laureijs et al. 2011; Euclid Collaboration et al. 2022, 2025) and LSST (Ivezić et al. 2019) will require full automation.

For a massive galaxy cluster like the Coma cluster with $M_{200} = 1.88 \times 10^{15} \, h^{-1} \, \mathrm{M}_{\odot}$ within $r_{200} = 1.99 \, h^{-1} \, \mathrm{Mpc}$ (Kubo et al. 2007), we expect that the galaxy population in the central region of the cluster is dominated by quenched galaxies with an early-type morphology including elliptical galaxies, S0 galaxies and dwarf spheroidal galaxies (e.g., Dressler 1980; Lewis et al. 2002; Gómez et al. 2003) that follow the red sequence (e.g., Visvanathan & Sandage 1977; Bower et al. 1992). Zöller et al. (2024) presented an automatic approach to detect cluster member galaxies using SExtractor (Bertin & Arnouts 1996) for the object de-

tection and separation of them from background objects based on quenched sequence membership in the u'-g' vs. g'-r' color-color diagram (Williams et al. 2009) and red sequence membership (Visvanathan & Sandage 1977). However, this study was based on images with significantly varying depth over the field and aimed for a clean sample rather than a complete sample using manual improvement of automatically created masks and manual fit rejection.

For this work, we obtained additional observations of the Coma cluster to achieve a larger field of view (FoV), and, more importantly, a homogeneous depth. Furthermore, we adjust the procedure presented in Zöller et al. (2024) for full automation of the dwarf galaxy cluster member selection and their structural parameter measurements, also allowing more interloping objects and then statistically correcting for contamination using the results from the identical analysis of two reference fields. Furthermore, we correct for completeness using an injection-recovery test.

Throughout this paper, we employ the cosmology calculator from Wright (2006), assuming a flat universe characterized by ${\rm H_0=69.6, km, s^{-1}, Mpc^{-1}}$ and $\Omega_m=0.286$ (Bennett et al. 2014), to determine the physical scales and distance moduli. For the Coma cluster, located at a redshift of z=0.0231 (Struble & Rood 1999), this yields a physical scale of 0.47 kpc arcsec⁻¹ and a distance modulus of 35.03 mag.

2. DATA

Our observations have been carried out with the Wendelstein Wide Field Imager (WWFI; Kosyra et al. 2014) at the 2.1 m-Fraunhofer Wendelstein Telescope (Hopp et al. 2014). The WWFI covers a field of view of $27.6' \times 28.9'$. It consists of four CCDs in a 2×2 mosaic and each CCD has 4096×4109 pixels with a pixel scale of 0.2 arcsec px⁻¹.

2.1. Sample and Observing Strategy

Our objective is to acquire deep u'-, g'-, and r'-band images of the Coma cluster with uniform depth in order to minimize sample selection biases. The u'-g'-r' color information is used to select the member galaxies (see Section 3.5). For this, we start with the data taken for the Coma cluster studies of the brightest cluster galaxy (BCG), intracluster light (ICL), and dwarf galaxies by Kluge et al. (2020, 2021) and Zöller et al. (2024). The dithering strategy for this archival data was optimized to measure the ICL around BCGs, and, therefore, delivers a large spatial coverage, allowing us to study the whole galaxy population in the Coma cluster. However, the depth is inhomogeneous. One full

Table 1. Coordinates of Pointing Centers

Pointing	R.A.	decl.
Coma Central	12:59:48	27:58:48
Coma Sky	12:56:38	28:08:27
Coma P0	13:01:48	27:31:48
Coma P1	13:01:48	27:58:48
Coma P2	13:01:48	28:25:48
Coma P3	12:59:48	28:25:48
Coma P4	12:57:48	28:26:49
Coma P5	12:57:48	27:58:48
Coma P6	12:57:48	27:31:48
Coma P7	12:59:48	27:31:48
Ref1 (SDSSJ1433+6007)	14:32:29	60:12:26
Ref2 (SDSSJ0909+4449)	9:10:11	44:45:58

dither pattern consists of 52 dither steps, as described in Kluge et al. (2020) and Zöller et al. (2024). The observations are centered between the two brightest galaxies in the Coma cluster, NGC 4874 and NGC 4889. For the first four exposures, the middle of the cluster is centered on each of the CCDs. Subsequent pointings are shifted by 2' in either the R.A. or decl. direction, repeating the four large dither steps in an off-center configuration. This full sequence is repeated 13 times. In addition, sky pointings were obtained between each of these dither steps to construct night-sky flats. The ICL of the Coma cluster spans nearly the entire field of view under the large dither pattern, making it impossible to derive accurate night-sky flats from the science exposures alone. Therefore, dedicated sky pointings are necessary.

This dither pattern was designed to optimize the background subtraction, but it does not provide a uniform depth, especially near the image corners. In order to obtain a more homogeneous depth and to increase the FoV, we took additional data with the same dither strategy at eight pointings around the central Coma pointing. The central coordinates of the different pointings are given in Table 1.

Furthermore, we observed two reference fields to investigate the sample contamination by interloping galaxies. For this, we chose a pointing around the lensed quasar SDSSJ1433+6007 (from now on referred to as Ref1) as we already had archival deep g'-band data available for the time-delay cosmography studies of this quasar (Queirolo et al. 2025) with additional u' and r' band data from Zöller et al. (2024). The other reference pointing is located around the lensed quasar SDSSJ0909+4449 (from now on referred to as Ref2).

For our reference pointings, we stick to the dither pattern applied by Queirolo et al. (2025). Here, we dither only 8" per dither step without centering the pointing on the different CCDs. This gives us a relatively uniform depth over a smaller FoV.

All observations were conducted under photometric conditions during dark time, with a zenith sky brightness fainter than $21.3 V \text{ mag arcsec}^{-2}$. Exposure times were chosen to ensure that sky photon noise dominated over readout noise. For the q' and the r' bands, we used $60 \,\mathrm{s}$ exposures in the fast readout mode. For the u' band, we opted for 600 s exposures in the slow readout mode, which reduces readout noise to about one-quarter with respect to the fast mode, albeit with a fourfold increase in readout time. For the g'-band observations of Ref1, Queirolo et al. (2025) used longer individual exposure times of 240 s. We emphasize that the different individual exposure times of the target and reference pointings have no considerable impact on the depth, as in both cases, the depth is limited by the photon noise of the sky. For each pointing, we took one full dither pattern (each 52 images) in the u' band, four full dither patterns in the g' band, and two full dither patterns in the r' band.

2.2. Data Reduction

The data was processed using the WWFI data reduction pipeline (Kluge et al. 2020; Kluge 2020), which incorporates fitstools (Gössl & Riffeser 2002), SExtractor (Bertin & Arnouts 1996), SCAMP (Bertin 2006), and SWarp (Bertin 2010). The pipeline performs various tasks, such as bias subtraction, flat-fielding, automatic masking of charge persistence, bad pixels, and cosmic rays. At the operating temperature of -115° C, dark current is negligible for the WWFI (Kosyra et al. 2014). Photometric zero-points for the q' and r' bands are determined by comparing the flux of point sources in 5" diameter apertures(ZP₅) to the Pan-STARRS DVO PV3 catalog (Flewelling et al. 2020). Our u'-band data is calibrated to the Sloan Digital Sky Survey (SDSS; York et al. 2000; Alam et al. 2015) photometric system because Pan-STARRS does not provide coverage in this

Afterward, we subtract extended point-spread function (PSF) models and ghosts from bright stars to improve the flatness of the background. For this, we subtract all stars contained in the GAIA EDR3 catalog (Gaia Collaboration et al. 2021) brighter than $14\,G$ mag. As the ghosts have some substructure at the level of a few percent that is not covered by the model, we additionally decided to mask all regions where the model exceeds 0.5 ADU in the g' and r' bands, and 10 ADU

in the u' band. Due to the large dither pattern and the resulting spatial shifts of the ghosts, as well as the number of individual exposures, the resulting masks do not remain in the final stack. As a consequence, the background, especially around the brightest stars, becomes more homogeneous. Therefore, we no longer need to mask large areas around the brightest stars.

Then, we create night-sky flats for each night, scale them to the individual exposures, and subtract them. For details, we refer to Kluge (2020)

In order to remove artifacts like satellite trails, reflections of stars at the edges of the CCDs, or nonmasked charge persistence, we use the robust clippedmean stacking method implemented in SWarp (Bertin 2010; Gruen et al. 2014) with $\sigma = 3$. However, this method only removes outliers that are 3σ above the background, and, hence, the outer PSF wings of satellite trails are not masked, and also faint parts of flares are not removed. Due to this issue, we developed an automatic method to remove those low-surface-brightness parts of artifacts. Manual masking of individual exposures, as it was done for Kluge et al. (2020) and Zöller et al. (2024) is not preferred anymore due to the large amount (≈ 4000) of individual images. As a basis for our masking method, we use the clip log file provided by SWarp and create from this log file a clipped-pixel mask for each individual resampled image. Then, we run a 3×3 pixel median filter over those images to remove individual clipped pixels. Afterward, we remove those with fewer than a thousand connected pixels, as satellite trails are considerably larger. The remaining masks contain mainly satellite trails, flares, and the centers of the brightest stars and their diffraction spikes. Then, we expand those remaining masks by convolving them with a circular tophat kernel with a diameter of 51 pixels, resulting in a more conservative mask covering also the low surface brightness features of the artifacts. Finally, the expanded mask is combined with the original clip-mask. These combined masks are then applied to the resampled images, their weights and error images, and then combined using the weighted average combination in SWarp. In Figure 1 we show a 10×10 times binned cutout of the Coma g' band stack without sigma clipping (left), with $3-\sigma$ -clipping applied (middle), and with our masking method applied (right). This method reliably removes the faint outer parts of bright artifacts. However, this method does not work for faint satellite trails when they do not exceed the clipping threshold. Those satellites are manually masked in the final stacks after visual inspection of 10×10 binned images.

Of all of the data taken, we reject some due to low sky transparency, bad seeing, stray light, light pollution,

Table 2. Exposure Times, Depths, and Seeing

		Coma	Ref1	Ref2
exp. time	u'	4940	570	570
(\min)	g'	1812	216	195
	r'	926	113	99
median	u'	30.0	30.0	30.0
3σ depth	g'	29.6	30.1	29.7
(mag arcsec^{-2})	r'	28.7	28.9	28.8
median	u'	1.15	0.93	1.10
FWHM	g'	0.96	1.17	1.08
(arcsec)	r'	0.95	1.03	1.07

NOTE—Total exposure time, median 3σ depth on a $10'' \times 10''$ scale, and median FWHM of our Coma cluster and the two reference field observations for the individual filter bands.

or significantly varying night-sky patterns. Additional observations were taken to account for that and to decrease the variation of the depth due to varying transparency and photon noise of the sky. However, we note that perfect homogeneity is not reached due to the limit of available observation time with the required observing conditions. The effect on our results is taken into account by an injection and recovery test (see Section 3.6).

Finally, all images are combined, and zero-points are determined for the stacks using a larger 10'' aperture. Additionally, new zero-points for the g' band are computed, taking into account the flux lost beyond the 10'' aperture following Kluge (2020):

$$ZP_{inf} = ZP_{10} + 0.1155 g' \text{ mag}$$
 (1)

Here, we only correct the g' band for this effect, as this correction factor is only available for this filter. Since the g' band serves as our reference measurement band and we use the u'- and r'-bands solely to derive aperture colors, this correction is not necessary for the latter. Unless otherwise specified, all g'-band total magnitudes and surface brightnesses are calibrated using $\mathrm{ZP}_{\mathrm{inf}}$. All colors and aperture magnitudes are calibrated using ZP_{10} . Magnitudes calibrated with ZP_{10} are consistent with those from Pan-STARRS (Kluge et al. 2020).

Additionally, a new astrometric solution is computed for the final stacks using the GAIA EDR3 catalog (Gaia Collaboration et al. 2021).

For the Coma cluster images, we finally restrict the area to $1.22\deg\times1.22\deg$, in order to yield a fairly homogeneous depth over the field of view, excluding the

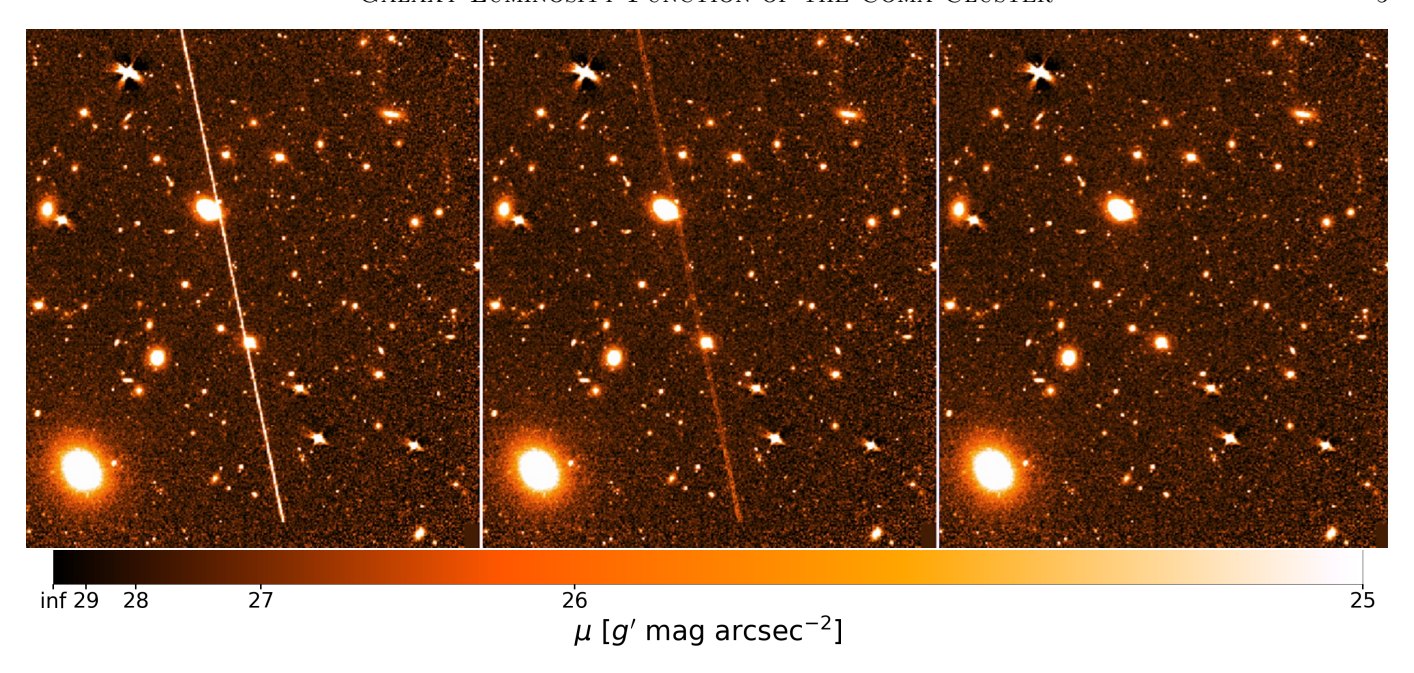


Figure 1. 10×10 times binned cutout of the Coma g' band stack created without sigma clipping (left), with $3 - \sigma$ -clipping applied (middle), and with our masking method applied (right).

low S/N regions in the outskirts. The resulting survey footprint is visualized as a color image in Figure 2.

The total exposure times and the median 3σ surface brightness depths, measured on a $10'' \times 10''$ scale, are listed in Table 2 for the Coma cluster stack and the reference fields across all filters. This depth indicates the surface brightness level at which a source with dimensions of $10'' \times 10''$ can be detected with 3σ confidence. The depths are calculated following Román et al. (2020):

$$\mu_{\text{lim}}(3\sigma; 10'' \times 10'') = -2.5\log\left(\frac{3\sigma}{\text{pxs} \times 10}\right) + \text{ZP} \quad (2)$$

where "pxs" is the pixel size in arcseconds. The depth maps for the Coma cluster and reference fields in the u', g', and r' bands are visualized in Figure 3, illustrating the achieved homogeneity.

3. DATA PROCESSING PIPELINE

In order to automatically identify and separate Coma cluster members from diffuse background galaxies and measure their structural parameters, we use the pipeline presented in Zöller et al. (2024) with a few improvements. In the following, we will give a brief overview of the pipeline; for details, we refer to Zöller et al. (2024). The basic pipeline includes accurate measurements of the PSF over the whole field of view using PSFEx (Bertin 2011).

Furthermore, we improve the flattening of the background by subtracting bright stars ($m \lesssim 16 \, g' \, \text{mag}$) us-

ing an extended PSF model, as well as models of the brightest three cluster galaxies NGC 4889 (including the ICL), NGC 4874, and NGC 4839.

To derive models for these galaxies, we use the isophote fitting tool isopy Kluge & Bender (2023); Kluge et al. (2023), which is based on the python package photutils (Bradley et al. 2020). Here, the ellipticity, position angle, and center of the isophotes can vary. Furthermore, disky- and boxiness are fitted and modeled. Beyond the largest fitted radius, all ellipse parameters are held fixed except for the radius. Model images are created by assigning the median measured flux value along these ellipses. For NGC 4889 and NGC 4874, we use masks from Zöller et al. (2024), and for NGC 4839, we create new masks using the same masking method to obtain masks for small and medium-sized objects and manually improve the masks. NGC 4889 and NGC 4874 are modeled iteratively, similar to the approach in Zöller et al. (2024) and Kluge et al. (2025). For that, we first apply the masks from Zöller et al. (2024), manually mask the fainter NGC 4874, and then create a first model of NGC 4889. This model is subtracted from the original stack, and the residuals are masked. Using the resulting image, the model of NGC 4874 is created and subtracted from the original stack, and the residuals are masked. Afterward, we create a second iteration model of NGC 4889. Then, the procedure is repeated to create a second version of the NGC 4874 model and a third iteration of the NGC 4889 model, which are also the fi-

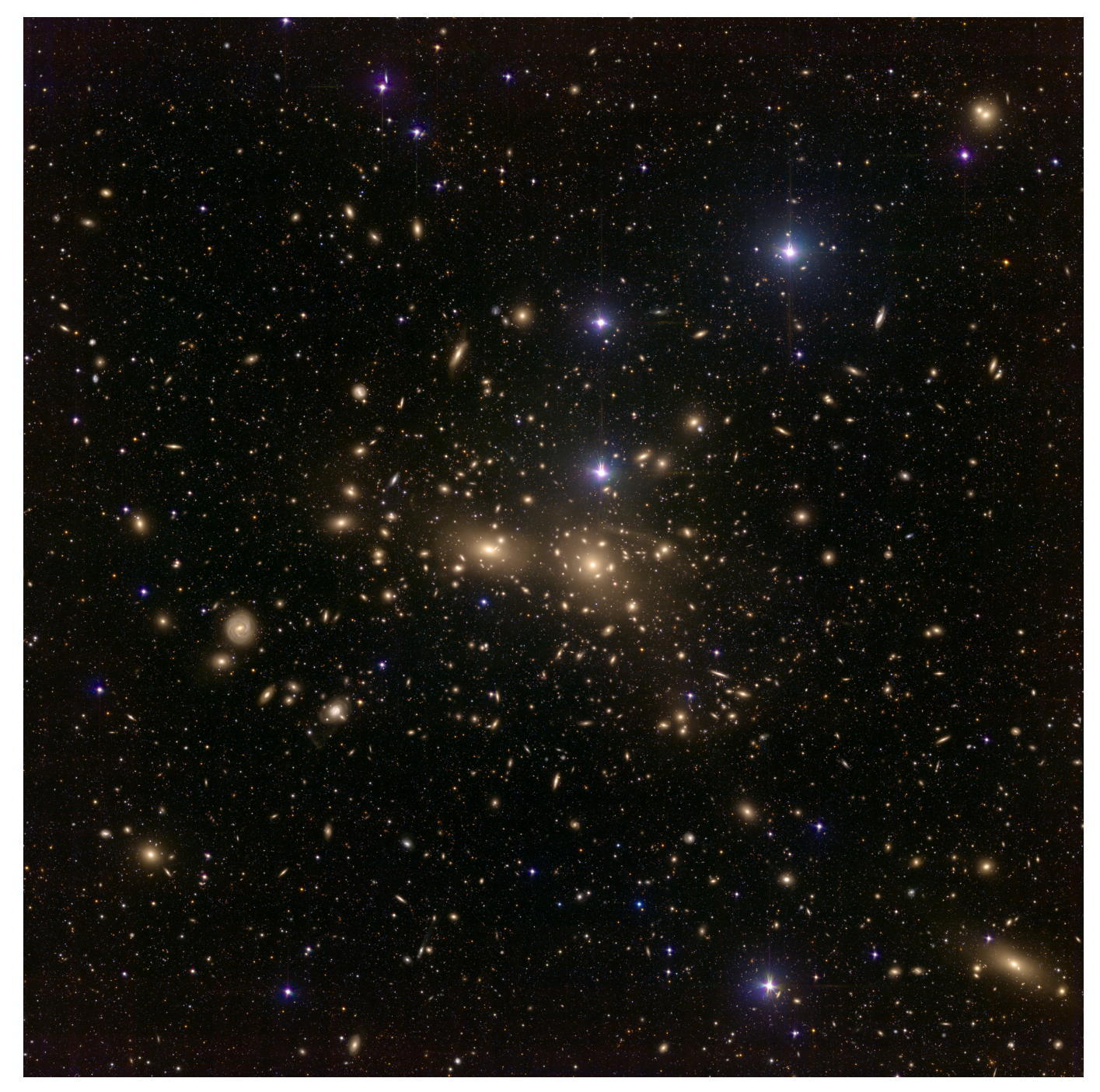


Figure 2. 6×6 binned u' - g' - r' color image of the Coma cluster survey region (1.22 deg \times 1.22 deg). Note that the bright star models were reinjected into the actual science stacks with one-third of their actual flux for visualization only.

nal models. For NGC 4839, no iteration is needed. The models of NGC 4889, NGC 4874, and NGC 4839 are subtracted from the star-subtracted image stack. Figure 4 shows color images of the center of the Coma cluster before (left) and after (right) the subtraction. The image demonstrates how the removal of NGC 4889 and NGC 4874 reduces contamination, enabling more accu-

rate detection and measurement of the underlying galaxies. Residuals are manually masked.

3.1. Object Detection

Source catalogs are created using SExtractor (Bertin & Arnouts 1996), detecting objects in the g' band images. The catalogs contain first estimates of the structural parameters and positions of the objects. They are

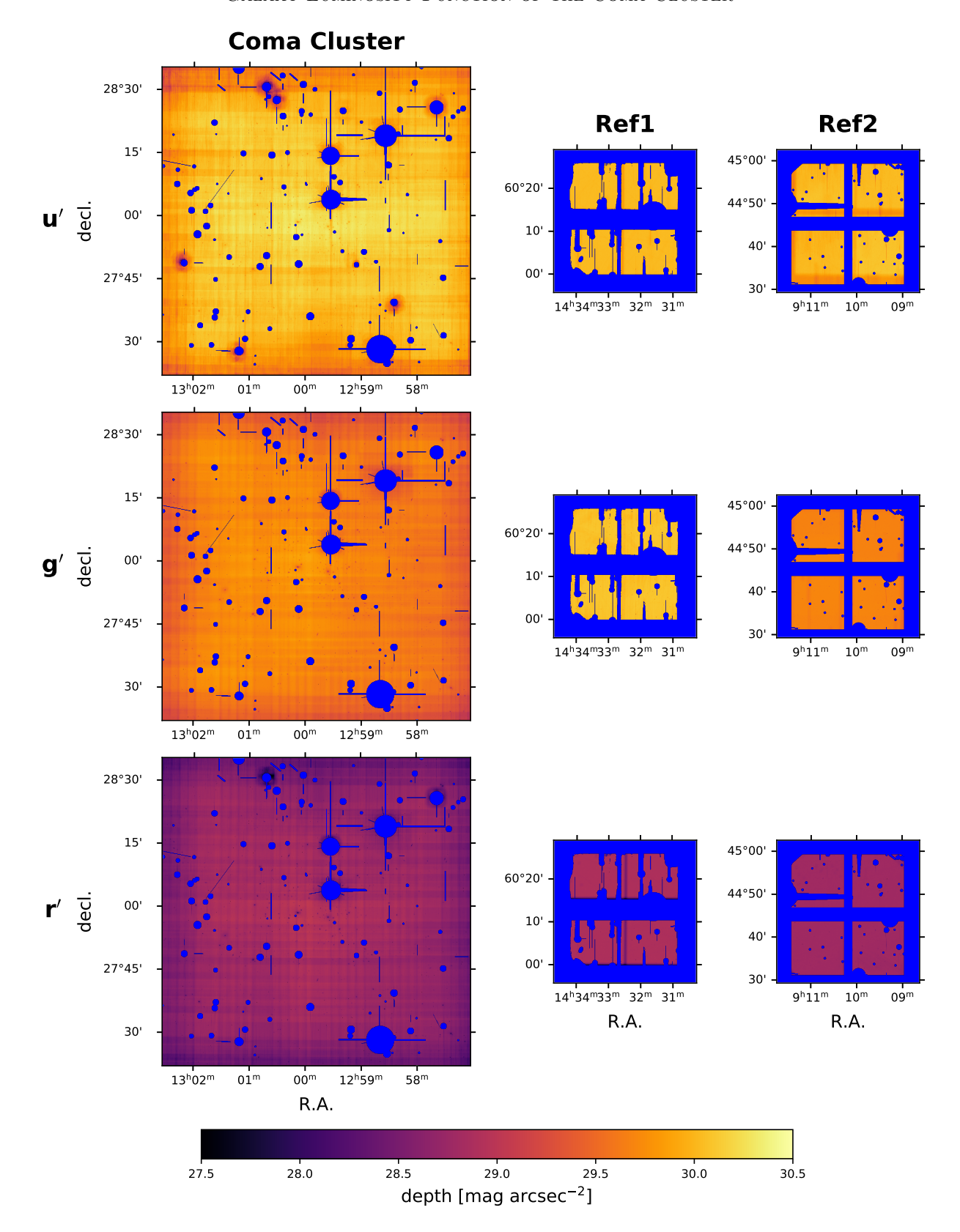


Figure 3. 3σ depth on a $10'' \times 10''$ scale of our Coma cluster data (left), as well as of our two reference fields Ref1 (middle), and Ref2 (right) in the u' (top), g' (middle), and r'-band (bottom).

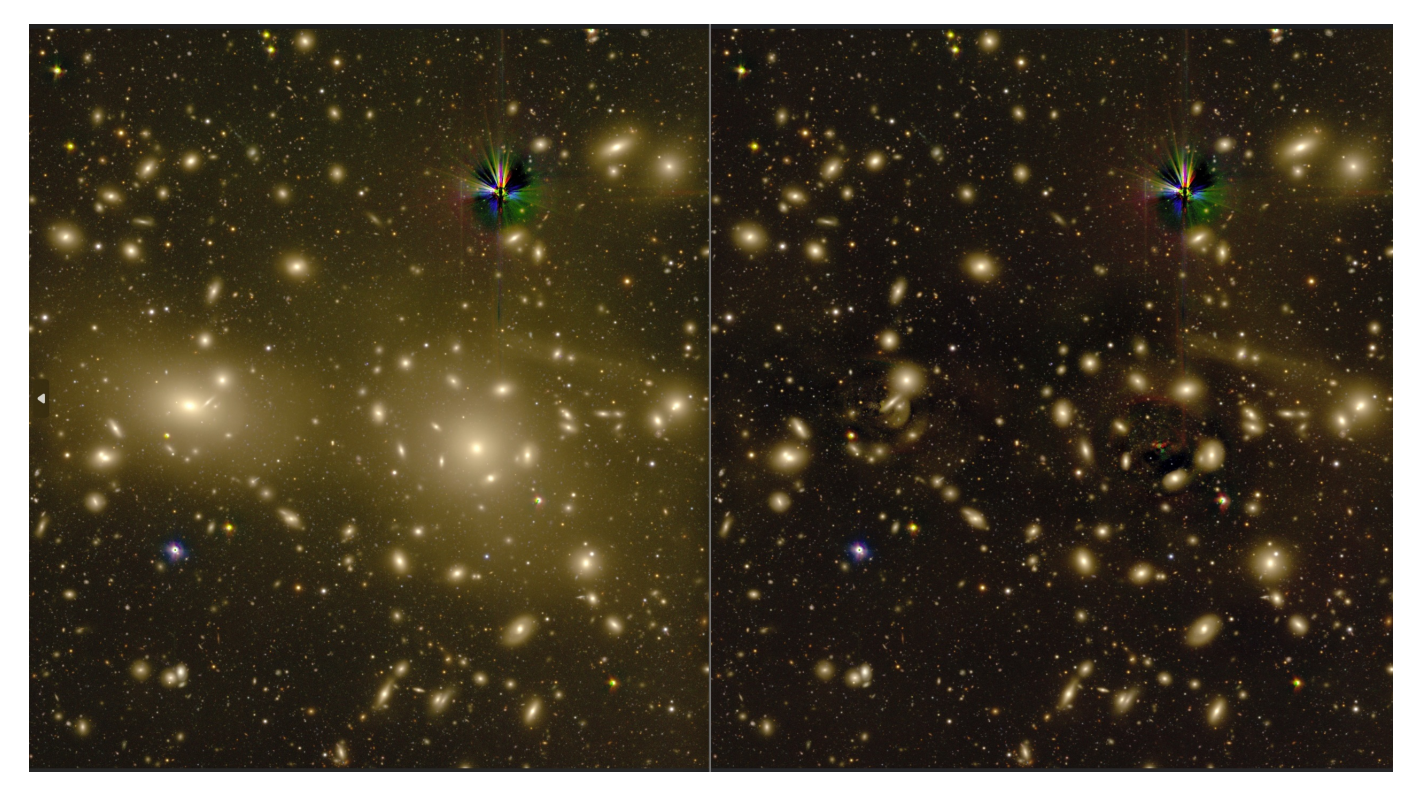


Figure 4. u' - g' - r' image of the central region of the Coma cluster before subtracting NGC 4889 (including the ICL) and NGC 4874 (left) and after (right).

in the following used to preselect cluster member candidates and as initial parameters for a more precise measurement using GALFIT (Peng et al. 2010). We create two object catalogs, one for large and bright sources and one for relatively small and faint sources, and combine them afterward. The SExtractor parameters for faint objects were optimized to reliably detect UDGs in the Coma cluster while avoiding obvious false detections. In this run, we employ smoothed images (convolved with a Gaussian kernel with $\sigma = 2 \,\mathrm{px} = 0.4 \,\mathrm{arcsec}$) to reduce false detections of noise peaks while simultaneously increasing the number of detected UDGs. The parameters for large objects were tuned for large elliptical galaxies. For an in-depth discussion of the creation of object catalogs, we refer to Zöller et al. (2024). Compared to Zöller et al. (2024), the Coma data has a more homogeneous depth, which allows us to slightly tweak the detection parameters of the SExtractor call for small objects. <code>DETECT_THRESH</code> was increased from $27.2\,g'\,\mathrm{mag\,arcsec^{-2}}$ to $27.6 \, g' \, \text{mag} \, \text{arcsec}^{-2}$, and the BACK_SIZE was increased from 32 px to 64 px.

3.2. Masking

To create individual object masks, we follow the masking procedure presented in Zöller et al. (2024). Here, a set of multiple masks covering different scales of objects

is combined while always demasking the central object. These individual masks were created using two methods. The first method is to strongly smooth the images and afterward mask connected pixels above a certain local threshold if their area exceeds the detection area. The second method involves running SExtractor with various detection parameters and background subtractions, and then utilizing the segmentation maps as masks. For details and the parameters used, we refer to Zöller et al. (2024).

In addition to those masks, we create a mask focused on faint point sources. This was necessary, as non-masked faint point sources were the main reason for manual masking in Zöller et al. (2024). Automatically masking them is especially problematic when they overlap with extended sources. Even if they are detected as individual objects, their segmentation maps can contain too much of the stellar body of a dwarf galaxy, and hence result in unnecessarily large masks. Therefore, we create another SExtractor segmentation map for the g' band with an aggressive background subtraction using BACK_SIZE=8, BACK_FILTERSIZE=3, DETECT_MINAREA=16, and a detection threshold of $27.2 \, g' \, \text{mag} \, \text{arcsec}^{-2}$. This SExtractor run uses the smoothed images to mitigate false detections and to create more conservative masks. This back-

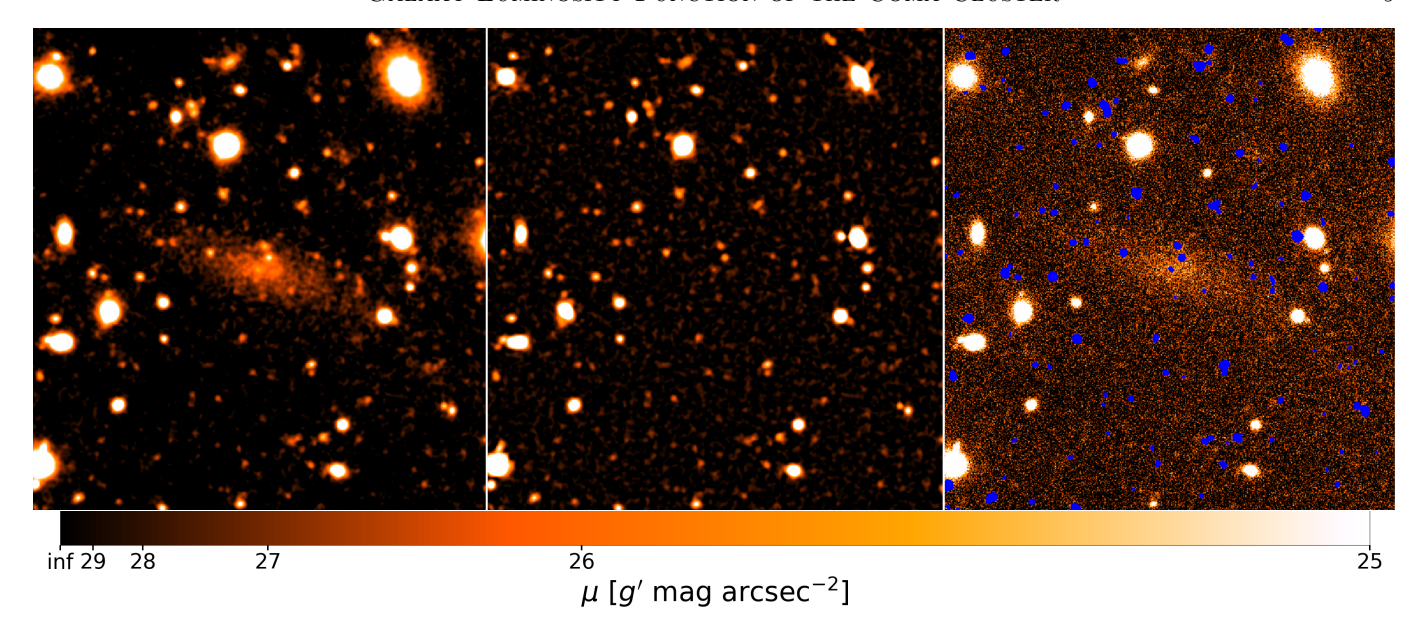


Figure 5. Smoothed g' band image before (left panel) and after (middle panel) the aggressive background subtraction. The created masks (blue) for faint point sources are shown in the right panel, applied to the non-smoothed image.

ground subtraction efficiently removes the outskirts of galaxies or even a whole diffuse galaxy such as DF15 (van Dokkum et al. 2015) as shown in Figure 5 (middle panel), allowing the detection and masking of faint point sources. We remove all masks containing more than 200 pixels, as this background subtraction also leads to artifacts around the centers of bright galaxies and does not provide proper masks for them, and because we only want to create a mask for faint point sources. The resulting mask applied to a non-smoothed cutout around DF15 is shown in blue on the right panel of Figure 5. These masks are expanded by a convolution with a tophat kernel of a diameter of 11 pixels during the creation of the individual object masks, after unmasking the central object in order to obtain more conservative masks. For bright galaxies, this saves significant time for manual masking, but the main benefit is for the fits of faint objects, as opposed to Zöller et al. (2024) we rely on full automation of the masking and fitting due to the enormous amount of fitted objects (see Section 3.4).

3.3. Modeling and Subtraction of Bright Galaxies

We aim to measure the luminosity function and structural parameter number densities of a large dynamical range of galaxy brightnesses in the Coma cluster, ranging from the BCG to the dwarf galaxy regime. However, these galaxies show very different morphologies. Most dwarf galaxies in galaxy clusters have a simple morphology that can be well modeled with a single Sérsic (1968) model, whereas brighter galaxies can be more compli-

cated. S0 galaxies consist of a bulge and a disk component, and elliptical galaxies frequently show isophote shifts and twists, have a varying ellipticity, differ from perfect elliptical isophotes (i.e., disky or boxy isophotes), or require multiple Sérsic components. Hence, we chose to use two different ways to model the galaxies. For dwarf galaxies, we use single Sérsic GALFIT (Peng et al. 2010) fits, and for brighter galaxies such as ellipticals, S0s, and spirals, we choose to use the more versatile isophote fitting approach using isopy Kluge & Bender (2023); Kluge et al. (2023). This approach also leads to fewer residuals than just fitting a simple single or double Sérsic profile. As automatically detecting dwarf galaxies that overlap with brighter galaxies is challenging, we also use these accurate isophote models to subtract the bright galaxies from the images to improve the detectability and the structural parameter measurements of such galaxies.

All objects with $(m \leq 18\,g'\,\mathrm{mag})$ and a star-galaxy classifier (S/G) lower than 0.4 are considered bright galaxies and modeled with isopy. For all objects, the masks are manually checked and improved. Using isopy, we measure the isophotes in the g' band, while allowing the central coordinates of the isophotes, ellipticity, position angle, and disky-/boxyness (a_4/a) to vary. The surface brightness (SB) of each isophote is updated for the u' and r' bands while keeping the isophotal shapes fixed to those measured in the g' band. The SB of each isophote is determined using the median flux, but in the case of an apparent spiral structure or star formation regions, the mean flux is used to avoid bias-

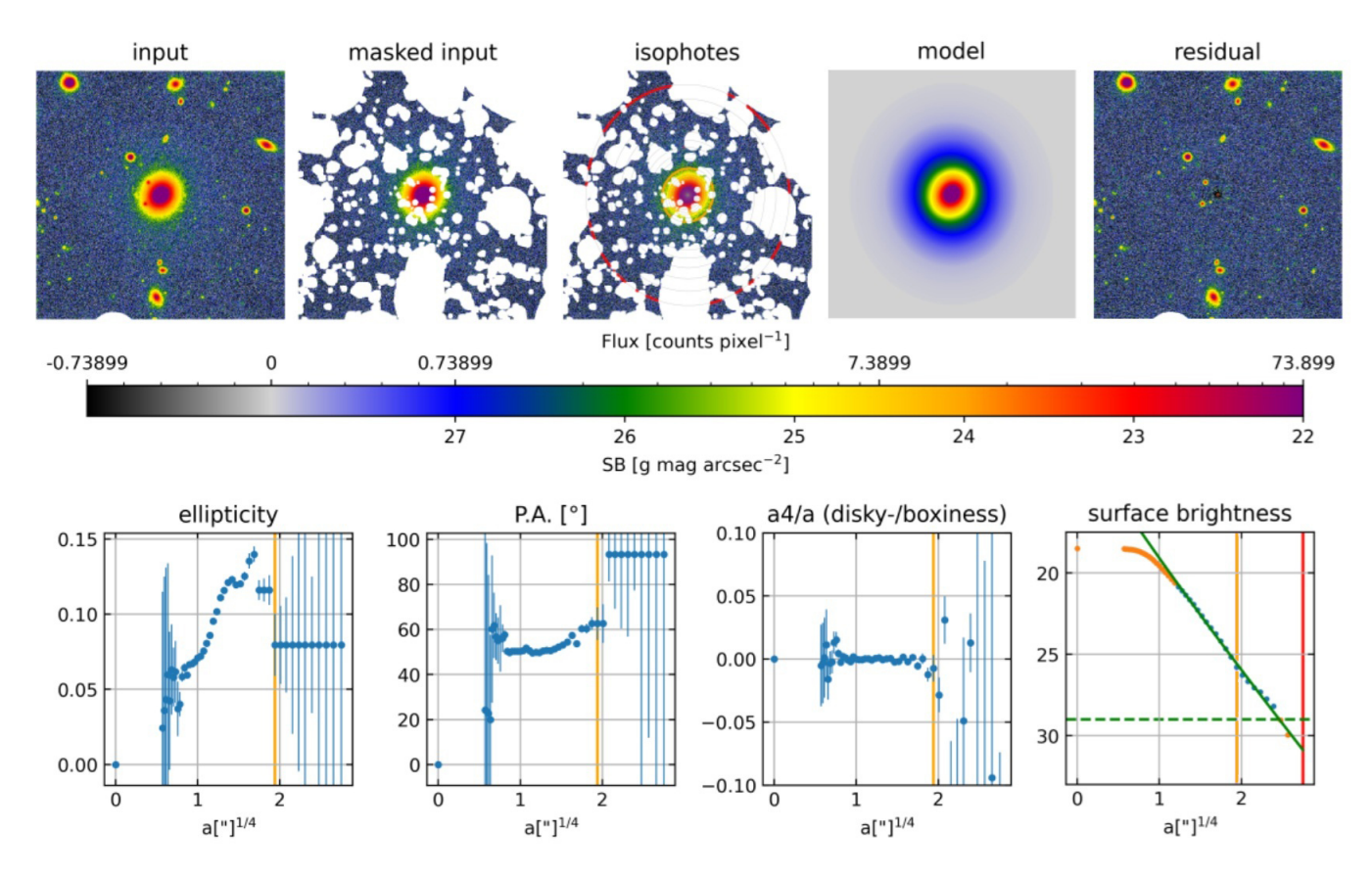


Figure 6. Selected outputs of the fitting routine for LEDA 44562 in the g' band. The ellipticity, position angle, and central coordinates are fixed after the orange marked isophote. The background is determined at the red-marked position. In the surface brightness profile plot, the green dots are the data points used for the fit, the solid green line corresponds to the best-fit Sérsic profile, and the dashed green line indicates the threshold from which the Sérsic profile is used as the model.

ing the measurement. To the measured SB profiles, we fit a single Sérsic function to the outer regions, avoiding the seeing-dominated center ($a < 2 \operatorname{arcsec}$). In the case where multiple components would be required to fit the profile, we manually restrict the fit to the surface brightness range of the outer component, as this is only required to extrapolate the outer flux, as in Kluge & Bender (2023). The measured SB profile and the Sérsic profile are combined at $29 \,\mathrm{mag}\,\mathrm{arcsec}^{-2}$ because of the strong scatter at low surface brightnesses. The structural parameters are then directly derived from these models. An example isopy output is shown in Figure 6. For some galaxies, we manually set the blending threshold to a brighter SB, to avoid a scatter in the model due to the uncertainties in the flux measurements of individual isophotes or to avoid an impact due to variations in the background (here also the fit ranges are adjusted accordingly). The latter is especially relevant for galaxies close to the centers of the brightest cluster galaxies that were subtracted before, as those galaxies can be affected by residuals of the subtraction. Furthermore, 10 pairs

of galaxies were modeled iteratively due to their strong overlap.

Finally, all models are subtracted from the images and residuals are manually masked. After that, the object detection is run again, and new automatic masks are created.

3.4. Modeling of Faint Galaxies

We preselect faint galaxy candidates with an apparent magnitude between $17\,g'$ mag and $27.2\,g'$ mag and a mean surface brightness within the effective radius between $15\,g'$ mag arcsec⁻² and $29.4\,g'$ mag arcsec⁻². The faint limits are set to mitigate false detections. Further false detections are mitigated by removing objects with FLAGS>4 or PETRO_RADIUS=0. Furthermore, we reject clear point sources from our sample with S/G>0.9 or $R_e < 2\,\mathrm{px} = 0.4\,\mathrm{arcsec}$, where R_e is the directly integrated half-light radius, which is not corrected for the PSF.

To model the fainter galaxies, we fit single Sérsic models to all galaxy candidates. Unlike in Zöller et al. (2024), we do not perform a manual check and remask-

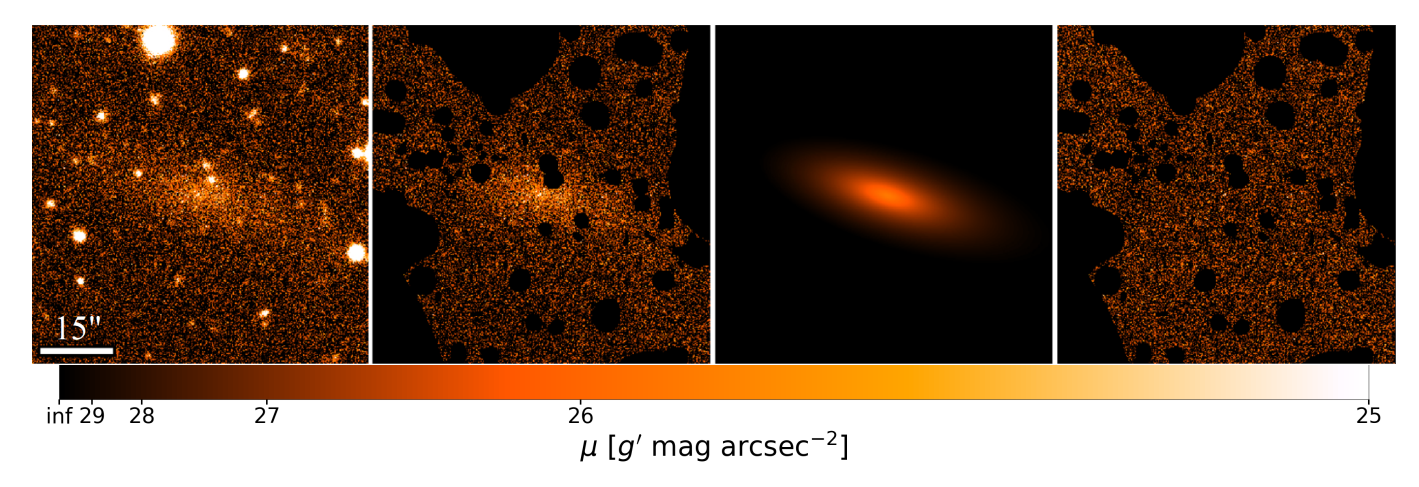


Figure 7. Unmasked cutout around the UDG DF15, the automatically masked image, the best-fit model, and the residual image (f.l.t.r.)

ing of the fits. The main reason is to avoid an observer bias, i.e., unintentionally creating better manual masks for the galaxies in the Coma image than for the reference images or manually rejecting fewer fit results, which could potentially lead to an incorrect completeness correction. Furthermore, Zöller et al. (2024) aimed for a clean sample, whereas we aim for a representative sample and statistically correct for contamination and completeness.

The masking and fitting procedure is adopted from Zöller et al. (2024) with some modifications. Briefly summarized, in each individual mask, the central object and all overlapping ones are demasked, and then the masks are combined. Afterward, all demasked objects contained in the SExtractor catalog are modeled simultaneously using GALFIT either with a Sérsic or a PSF model. The colors of the objects are measured using elliptical apertures after subtracting the local background and convolving the cutouts in the different filter bands to the same target PSF. In Figure 7, we show the extreme example of the UDG DF15 (van Dokkum et al. 2015) which exhibits a very low surface brightness, extremely large extent and a lot of contamination that needs to be masked. Here, we show from left to right the unmasked cutout around DF15, the automatically masked image, the best-fit GALFIT model with $R_e = (9.9 \pm 0.6) \,\mathrm{kpc}$, $M = (-15.70 \pm 0.06) \,g' \,\mathrm{mag}$, $n = 1.10 \pm 0.06, \ \mu_e = (27.53 \pm 0.08) \ g' \, \text{mag} \, \text{arcsec}^{-2},$ and $\mu_0 = (25.48 \pm 0.05) \, g' \, \text{mag} \, \text{arcsec}^{-2}$, as well as the residual image.

As we do not perform any additional manual remasking, we improved the automatic masking compared to Zöller et al. (2024), focusing on the main issues that required manual remasking. The first improvement is an additional mask for faint point sources as described

in Section 3.2. Furthermore, we increased the mask sizes by convolving them with a tophat kernel with a diameter of 7 px after the demasking process. An issue that remains is objects that were not deblended by SExtractor. This affects the galaxies that we inject for the injection and recovery test (Section 3.6) equally, and therefore is statistically corrected. However, for individual objects, the results of Zöller et al. (2024) can be more accurate.

The resulting catalogs are processed analogous to Zöller et al. (2024), rejecting objects with large uncertainties ($\Delta(u'-g')>0.2\,\mathrm{mag}$, $\Delta(g'-r')>0.2\,\mathrm{mag}$, $\Delta m>1\,g'\,\mathrm{mag}$, $\Delta\mu_0>1\,g'\,\mathrm{mag}\,\mathrm{arcsec}^{-2}$, $\Delta\mu_e>1\,g'\,\mathrm{mag}\,\mathrm{arcsec}^{-2}$, or $\Delta R_e/R_e>0.5$). Furthermore, we correct for galactic extinction (Schlafly & Finkbeiner 2011) and, assuming that objects are at the distance of the Coma cluster, we apply K-correction (Chilingarian & Zolotukhin 2012), and calculate absolute magnitudes using the distance modulus and cosmic dimming obtained from the cosmology calculator by Wright (2006). For more details, we refer to Zöller et al. (2024).

3.5. Cluster Member Candidate Selection

First, we preselect quiescent galaxies using a u'-g' versus g'-r' color–color selection. Here, we use the effect that the 4000 Å break in quenched galaxies separates the star-forming galaxies and the quenched galaxies in color–color space (Williams et al. 2009). We adjust the selection cutoffs from Zöller et al. (2024) by shifting them by 0.2 mag in u'-g' to include also transitioning galaxies from the star-forming sequence to the quenched sequence and only exclude clear star-forming galaxies.

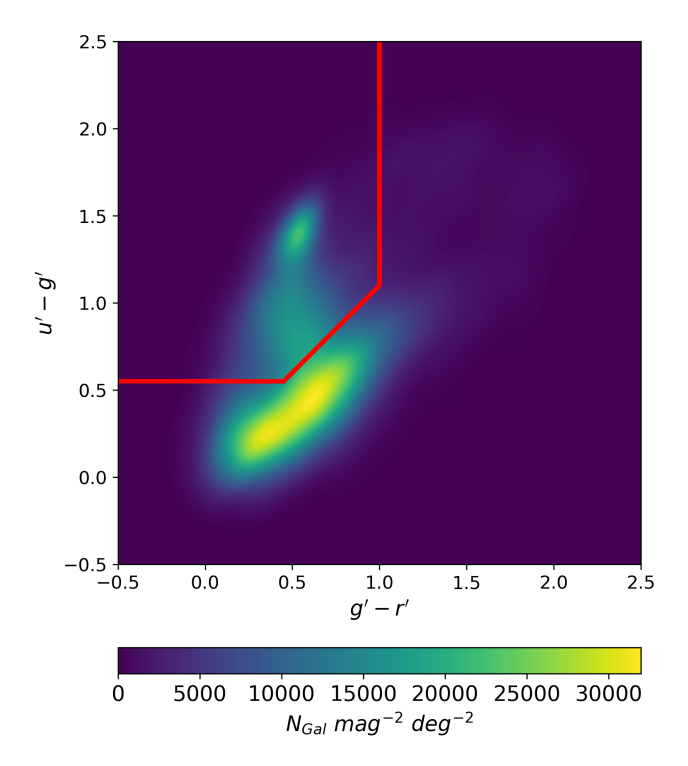


Figure 8. u' - g' vs. g' - r' number density color-color diagram for the Coma cluster. Galaxies in the top left of the red visualized selection cutoffs are considered to be quenched.

The selection criteria are given by:

$$u' - g' > g' - r + 0.1 \tag{3}$$

$$u' - q' > 0.55 \tag{4}$$

$$q' - r' < 1 \tag{5}$$

In Figure 8, we show the selection cuts as a red line overlayed on the number density of galaxies in the color-color diagram. The galaxies in the top left corner are categorized as quenched.

Furthermore, we use the g'-r' red sequence to improve the purity of the cluster member selection. To determine the red sequence, we determine the ridge of a Gaussian Kernel Density Estimate (KDE) in the g'-r' vs. $m_{g'}$ space. For this, we calculate the KDE maxima in bins of $0.75\,g'$ mag. Here, we use all bright galaxies and the preselected quiescent galaxies with $m_{g'} < 23.2\,g'$ mag, as well as only bins containing at least 10 objects. Using linear regression, we fit the red sequence to those maxima of the magnitude bins, giving a red sequence with:

$$g' - r' = (-0.023 \pm 0.001) \times m_{g'} + (1.03 \pm 0.02)$$
 (6)

To determine the red sequence members, we assume an intrinsic red sequence width of $3\sigma \approx 0.1 \,\mathrm{mag}$ (Kluge

et al. 2024). Objects that deviate by less than $3 \times \Delta(g'-r')$ from the intrinsic red sequence are considered cluster member candidates. This will also include more contamination than the selection in Zöller et al. (2024), which used a 2σ intrinsic width, but here our objective is to obtain a more complete sample and correct for contamination statistically (see Section 3.7). The red sequence selection is visualized in Figure 9, with the maxima of the KDE bins displayed as black dots, the best-fit red sequence as the solid black line, and the limits of the 3σ intrinsic red sequence as dashed black lines. Galaxies considered to be cluster member candidates are depicted in red, and those that are removed in the red sequence selection are shown in blue. In total, we find 4829 Coma cluster member candidates in the faint sample.

3.6. Completeness Function

Correcting for the completeness of the sample is crucial for determining the GLF. For the bright galaxy sample, we assume 100% completeness in the unmasked areas, as such bright objects are easily detected by SExtractor, and in the modeling process (Sec. 3.3), we successfully measured their structural parameters for the entire bright sample. To derive the completeness function of our faint galaxy sample, we perform an injection-recovery test. For this, we randomly draw the structural parameters from our final Coma faint galaxy sample, generate single Sérsic mock galaxies, convolve them with the local PSF, add the photon noise of the galaxy, and inject them onto a grid with a step size of 500 px into the science frame. Here, we do not add the photon noise of the sky, as it is already in the science stack.

Then, we run the pipeline again, starting at the SExtractor run for faint objects. We count all galaxies that we find within 1 arcsec that are retained in the final catalog as being recovered. We also classify as unrecovered any galaxies whose recovered magnitude is more than $0.75\,g'$ mag brighter than the injected value (i.e., a factor of ≈ 2 in total flux), as these are likely mismatches with another object.

We model the completeness function using a 3rd order polynomial function. We clip the completeness polynomial to values between 10^{-6} and $1-10^{-6}$ to avoid undefined values in the log-likelihood computation. Note that the completeness for galaxies fainter than the clip-off magnitude is not exactly zero, since a few are detected in the science image. However, as the completeness is very low in this regime and the completeness correction is not trustworthy, we decide to limit our sample to brighter magnitudes than this clip-off magnitude. To derive the best-fit parameters of the polynomial, we

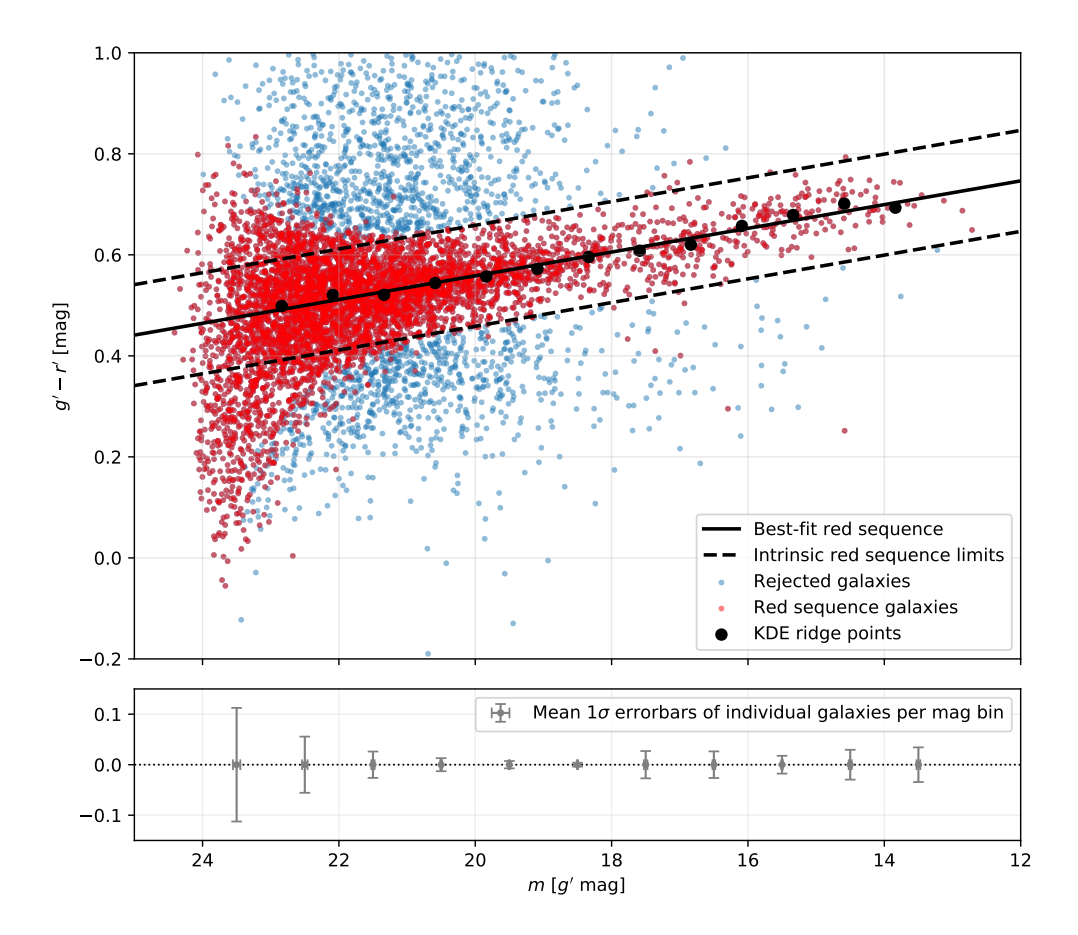


Figure 9. g'-r' color-magnitude diagram of the Coma cluster. The KDE ridge points are depicted as black dots, the best-fit red sequence as a solid black line, and the limits of the intrinsic red sequence as dashed black lines. Galaxies that deviate more than $3 \times \Delta(g'-r')$ from these limits are removed from the sample. The galaxies rejected by this red sequence selection are visualized in blue, and those that are accounted as cluster member candidates are shown in red. In the bottom panel, we visualize the typical errorbars of the individual galaxies within a magnitude bin. Note here that the colors of the faint galaxy sample were measured using aperture magnitudes and hence their uncertainties only include photon noise and the uncertainty of the background subtraction, whereas the colors of the bright sample $(m < 18 \, g' \, \text{mag})$ are based on the SB profile modeling of the whole galaxy and hence also includes the modeling uncertainties causing larger errorbars.

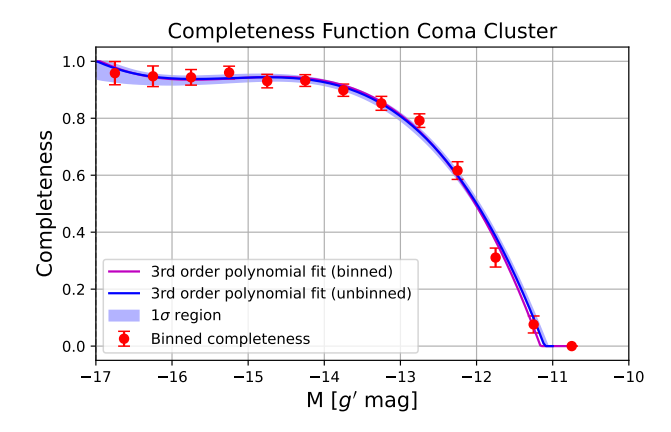


Figure 10. Completeness Function Coma Field

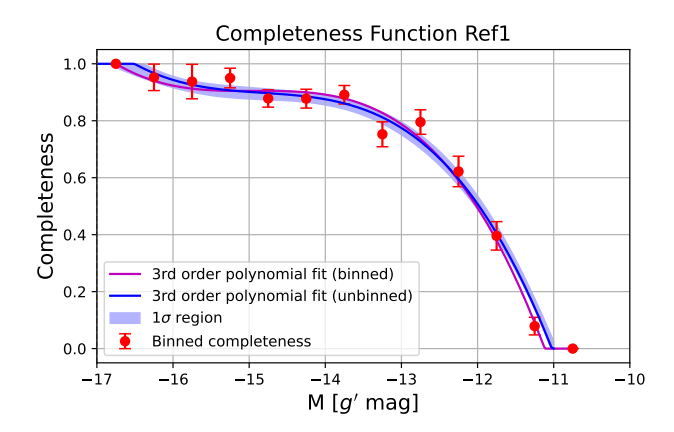
derive the Bayesian posterior distribution and the bestfit parameters using the dynamic nested sampling package DYNESTY (Speagle 2020). We use a Bernoulli distribution for the injection recovery test:

$$\mathcal{L} = p^k (1 - p)^{1 - k} \tag{7}$$

Here, we use the unbinned data from the injection recovery test, where k = 1 is recovered and k = 0 is not recovered, compute a log-likelihood for each galaxy magnitude (M_i) , and derive the joint log-likelihood:

$$\ln \mathcal{L} = \sum_{i} k_i \ln\{p(M_i)\} + (1 - k_i) \ln\{1 - p(M_i)\} \quad (8)$$

To inform the priors for the nested sampling, we use the results from a least-squares fit to the binned data points



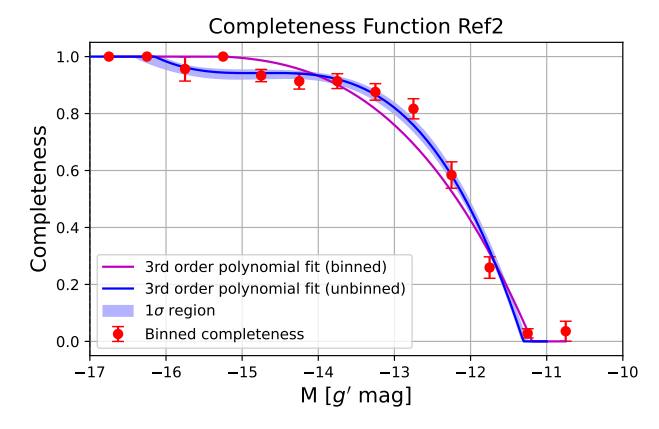


Figure 11. Completeness Functions Reference Fields

with a bin width of 0.5 mag. In Figure 10, we show the derived completeness function for the Coma cluster, with the binned data points overlayed for visualization. We find a relatively flat completeness function in the range of $-16\,g'\,\mathrm{mag} \lessapprox M \lessapprox -14\,g'\,\mathrm{mag}$, reaching about 100% at the bright end, and dropping fast for $M \gtrapprox -13\,g'\,\mathrm{mag}$.

3.7. Contamination: Reference Fields

To probe the contamination of our Coma cluster galaxy sample, we run the pipeline on the reference fields. Here, we only adjust the galactic extinction correction and use exactly the same color–color and color–magnitude selection as for the Coma cluster. Furthermore, we assume that all found objects would be at the distance of the Coma cluster, regardless of their true distance, as also done for the contamination contained in the Coma sample. For Ref1, the final faint galaxy sample contains 152 galaxies, and for Ref2, it contains 144 galaxies.

To derive the completeness function for the reference fields, we follow the approach presented before. Here, we draw random galaxies from the catalogs of both reference fields. For the reference fields, we perform the injection recovery test five times. The first four times, we draw from the whole sample and inject them onto a grid with a step size of $500\,\mathrm{px}$, with the grid being shifted by $250\,\mathrm{px}$ in the x or y direction for each injection. Due to the low number of relatively bright galaxies in the reference field catalogs, we did a fifth run, randomly drawing only galaxies with $M<-14\,g'$ mag to improve the statistics for the completeness function at the bright end. The resulting completeness functions are displayed in Figure 11. For the reference fields, we find a similar shape of the completeness function as for the Coma field but with the Ref1 field reaching fainter magnitudes than the other two fields, presumably due to it's slightly higher depth in the g' band.

4. RESULTS AND DISCUSSION

4.1. Luminosity Function

The goal of this work is to determine the GLF of the Coma cluster. To derive the GLF, we want to use the unbinned data point, as the best-fit GLF derived by a fit to binned data points is sensitive to the chosen bin width and bin centers. This is especially affecting the bright end of the GLF due to the expected steep decline, and relatively low number of counts per bin. Hence, we want to use a maximum likelihood estimation using nested sampling based on the individual data points. However, we first measure the GLF using binned data points to inform the Gaussian prior for the nested sampling. Here, we correct the raw bin counts (black data points in Figure 12) with the best-fit completeness function and subtract the binned completeness corrected data points from the reference fields. For this, we use only galaxies with a detection probability larger than 5\%, i.e. $M < -11.3 \, g' \, \text{mag}$. Furthermore, we exclude the three brightest galaxies NGC 4889, NGC 4874, and NGC 4839 (light blue), which is often done in the literature because the GLF flattens in this regime and is not well described by a Schechter nor double Schechter function (e.g., Lin et al. 2004; Cuillandre et al. 2025). The completeness corrected bins are overlayed in turquoise, and the completeness and contamination corrected bins in blue. We note here that at the magnitude $(M \approx -17 \, g'\text{mag})$ where the sample is split into a bright and a faint galaxy sample, we do not find any indication of an offset implying that the two methods are consistent. The shape of the binned data points indicates that a single Schechter function is not sufficient to fit the GLF, but a double Schechter function is required to fit the GLF well. Hence, we perform a least-squares fit of a double Schechter function (Equation 9) to the completeness and contamination corrected bins (blue).

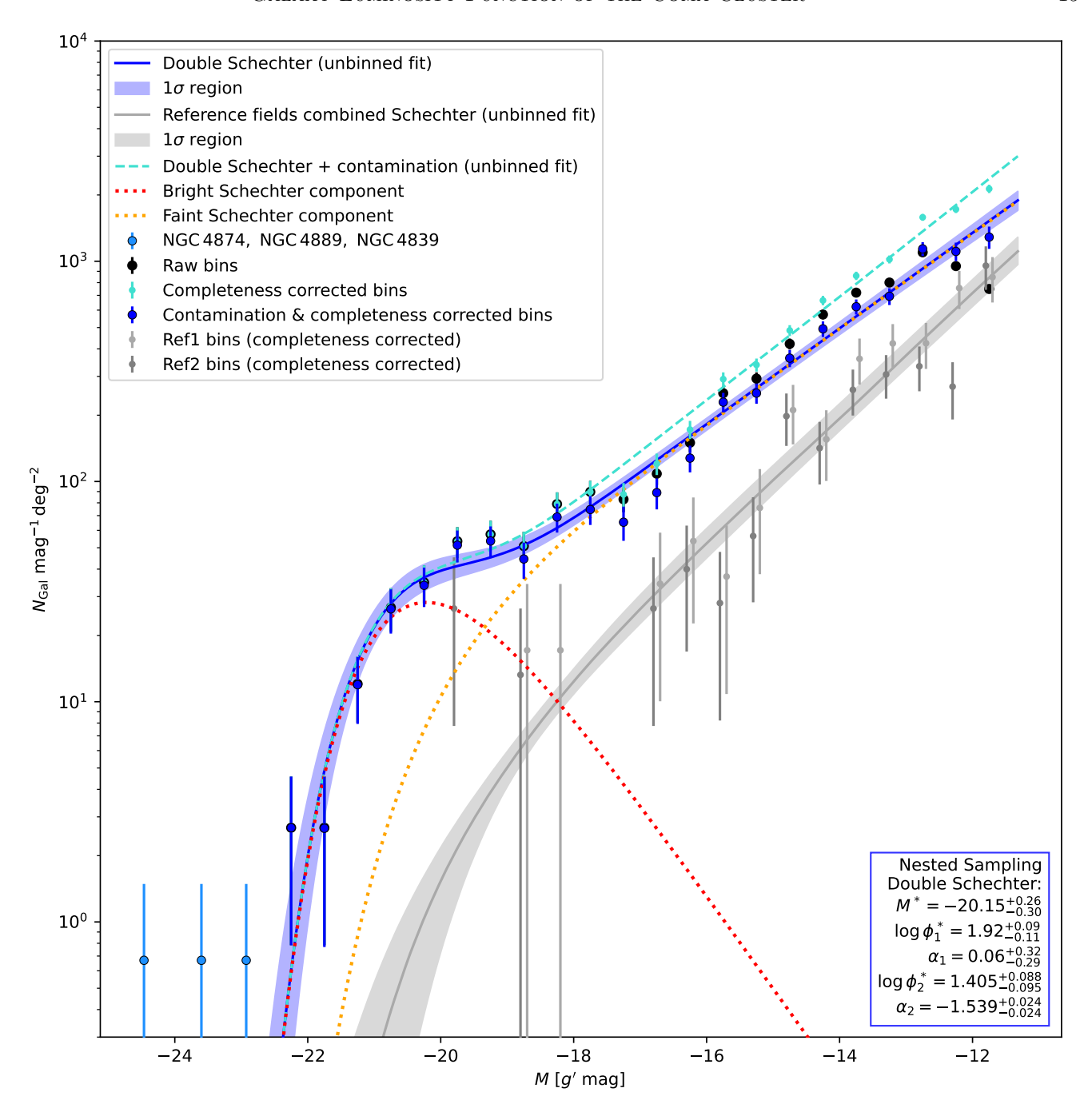


Figure 12. The best-fit GLF of the Coma cluster is visualized as a blue solid line with its 1σ uncertainty interval in shaded blue. The bright component of the best-fit double Schechter function is depicted as dotted red line and the faint component as dotted orange line. The completeness corrected counts per bin of galaxies from the reference fields are shown as light-grey data points for Ref1 and as dark-grey data points for Ref2 with their best-fit Schechter function as a solid grey line with its 1σ uncertainty interval in shaded grey. The Coma cluster raw counts per bin are visualized as black points, with the completeness corrected bin counts overlayed in turquoise and the completeness and contamination corrected bin counts in blue. The errorbars are given by σ_{Poisson} for the raw counts, $\sqrt{\sigma_{\text{Poisson}}^2 + \sigma_{\text{compl.}}^2}$ for the completeness corrected counts, and by $\sqrt{\sigma_{\text{Poisson}}^2 + \sigma_{\text{compl.}}^2} + \sigma_{\text{BG}}^2$ for the completeness and contamination corrected counts. Here, σ_{BG} is the uncertainty of the combined Schechter fits for the two reference fields, including the uncertainty from cosmic variance. For the bright and mediocre bins, the Poisson noise is dominating the uncertainties, and at the faint-end, σ_{BG} becomes dominant, whereas the uncertainty of the completeness correction is always minor. The dashed turquoise line indicates GLF in the Coma field, consisting of the best-fit GLF of the Coma cluster and the expected contamination. The three brightest galaxies, NGC 4889, NGC 4874, and NGC 4839, are shown in light blue and are not included included for the double Schechter fit. Their data points are not binned but shown at their actual positions.

$$\Phi_{\mathcal{C}}(M) = 0.4 * \ln 10 \times \exp\left[-10^{-0.4(M-M^*)}\right] \times \left[\Phi_1^* 10^{-0.4(M-M^*)(\alpha_1+1)} + \Phi_2^* 10^{-0.4(M-M^*)(\alpha_2+1)}\right]$$
(9)

For deriving the GLF of the Coma cluster using an unbinned maximum likelihood estimator, we require an analytic description for the contamination. For this, we fit a Schechter function (Equation 10) to the unbinned reference field data. Here, we fit a Schechter function to each of the reference fields individually to get an estimate for the cosmic variance. Afterward, we combine the normalized posterior distributions.

$$\Phi_{\rm BG}(M) = 0.4 * \ln 10 \times \exp\left[-10^{-0.4(M - M_{\rm BG}^*)}\right] \times \left[\Phi_{\rm BG}^* 10^{-0.4(M - M_{\rm BG}^*)(\alpha_{\rm BG} + 1)}\right]$$
(10)

To perform the maximum likelihood estimation, we again use the dynamic nested sampling package DYNESTY (Speagle 2020). We use a Poisson log-likelihood that is, following Cash (1979), given by:

$$\ln \mathcal{L} = -\mu + \sum_{i} n_i \ln \{f(M_i)\}$$
 (11)

where μ is the total expected number of counts and $f(M_i)$ is the finite expected number of counts at M_i . n_i is the number of counts per bin, but as we want to perform the fit using the unbinned data and get the luminosity function normalized by the area in units per deg², we use $n_i = 1/A$, where A is the respective covered area. For deriving the luminosity function of the background objects $\Phi_{\rm BG}(M)$, we use the following joint log-likelihood, accounting for the completeness function in the reference fields $C_{\rm BG}$:

$$\ln \mathcal{L} = -\int_{M_{\text{min}}}^{M_{\text{max}}} C_{\text{BG}}(M) \Phi_{\text{BG}}(M) dM$$
$$+ \sum_{M_{\text{BG}}} \frac{\ln \{ C_{\text{BG}}(M) \Phi_{\text{BG}}(M_{\text{BG}}) \}}{A_{\text{ref}}}$$
(12)

In the reference fields, we only found a small number of bright galaxies and hence, we can not determine the bright-end cut-off of well. We show the number count per bin in the reference fields in light-grey (Ref1) and dark-grey (Ref2), shifted by ± 0.05 mag for visualization. Note here that multiple of the magnitude bins of the reference fields have 0 counts. Hence, we assume that $M_{\rm BG}^*$

is similar to M^* derived from the binned Coma GLF fit and use this as a Gaussian prior with $\sigma=0.5\,\mathrm{mag}$. For Φ_{BG}^* , and α_{BG} , we use flat priors.

The posterior distribution is then derived using DYNESTY for each reference field. In order to take into account the uncertainty of the completeness function, we derive the posterior distribution of the Φ_{BG} fit 1000 times for each reference field, each time drawing new completeness function parameters from the posterior distribution of the completeness function fit (Section 3.7). We normalize each of the posteriors, combine them to a total posterior, and derive the best-fit parameters from that total posterior distribution. The resulting GLF of the reference fields is visualized as a grey line with a shaded area indicating the 1σ uncertainty in Figure 12. The total posterior distribution is shown in Figure 13. For both reference fields, the faintend slope matches well. For $M_{\rm BG}^*$ and $\log_{10}(\Phi_{\rm BG}^*)$, we find a bimodal distribution. As mentioned before, M_{BG}^* is generally not well defined due to the low number of bright galaxies in the reference fields. The difference in $\log_{10}(\Phi_{BG}^*)$ between the two reference fields, we interpret as cosmic variance. For Ref1 we find $\log_{10}(\Phi_{BG}^*)$ $0.85^{+0.16}_{-0.17}$ and for Ref2 we find $\log_{10}(\Phi_{BG}^*) = 0.40^{+0.14}_{-0.15}$. From the combined posterior, we derive median values of $\log_{10}(\Phi_{\mathrm{BG}}^*) = 0.60_{-0.27}^{+0.33}$ and $\alpha_{\mathrm{BG}} = 1.703_{-0.029}^{+0.029}$, which takes into account the uncertainty due to cosmic variance based on these the reference fields.

For the GLF of the Coma cluster, we follow a similar procedure. The joint log-likelihood for the nested sampling maximum likelihood estimate is given in Equation 13. Here, $f(M_i)$ consists of the expected counts of the Coma cluster itself and the expected counts of interloping background galaxies given the completeness function of the Coma cluster image C(M). Because the faint galaxies are detected on the images after subtracting the models of the bright galaxies and masking the residuals, the effective area in which the faint galaxies are detected (A_f) is smaller than the area of the bright sample $(A_{\rm b})$. Hence, we split the sum in the joint loglikelihood into our bright galaxy sample and our faint galaxy sample, and divide them by their respective effective area. The joint log-likelihood used to determine the GLF of the Coma cluster $(\Phi_{\rm C}(M))$ is given by:

$$\ln \mathcal{L} = -\int_{M_{\text{min}}}^{M_{\text{max}}} C(M)(\Phi_{\text{C}}(M) + \Phi_{\text{BG}}(M)) dM$$

$$+ \sum_{M_f} \frac{\ln\{C(M_{\text{f}})(\Phi_{\text{C}}(M_{\text{f}}) + \Phi_{\text{BG}}(M_{\text{f}}))\}}{A_{\text{f}}}$$

$$+ \sum_{M_b} \frac{\ln\{C(M_{\text{b}})(\Phi_{\text{C}}(M_{\text{b}}) + \Phi_{\text{BG}}(M_{\text{b}}))\}}{A_{\text{b}}}$$
(13)

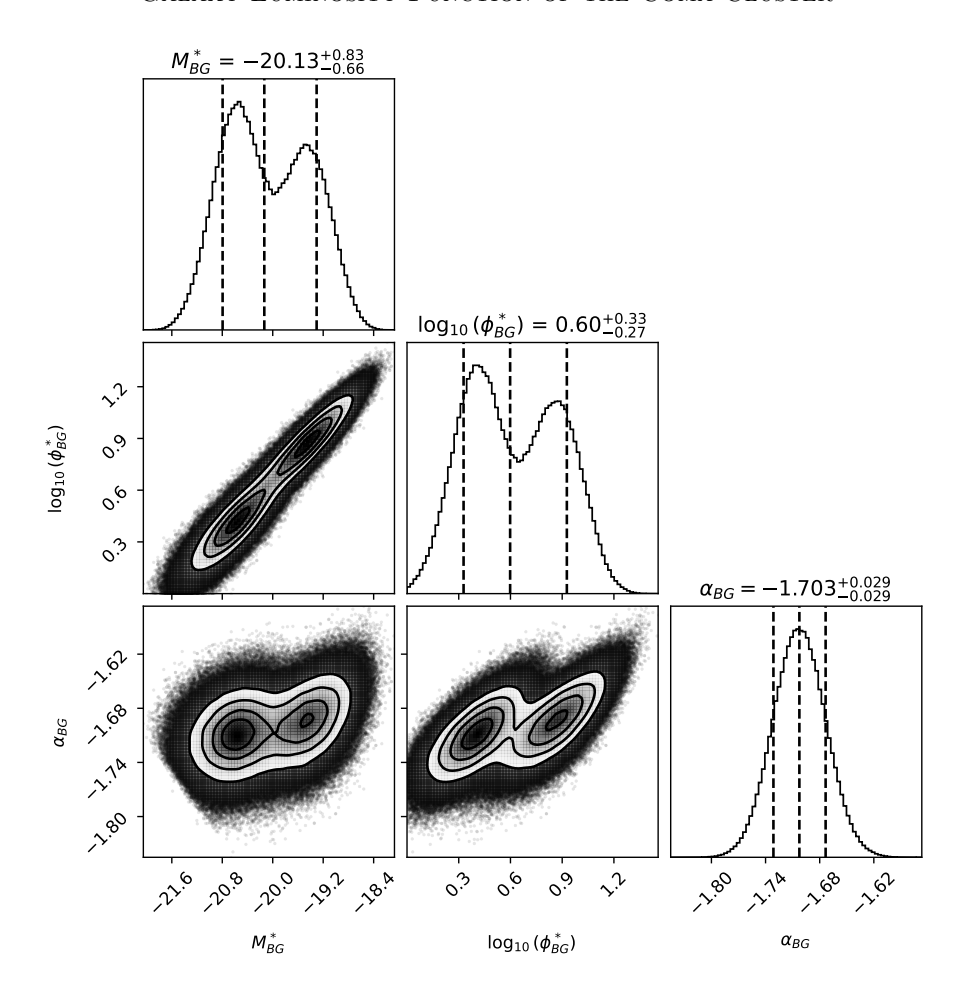


Figure 13. Combined posterior distribution of the fits of a GLF using a Schechter function for both reference fields individually. The contours correspond to the 0.5σ , 1σ , 2σ , and 3σ levels.

We propagate the uncertainties again by running the nested sampling 1000 times, randomly drawing the parameters for C(M) and $\Phi_{\rm BG}$ from their posteriors, normalizing the resulting posteriors, combining them, and deriving the best-fit parameters from the resulting total posterior. Note here that C(M) and Φ_{BG} are independent. The resulting total posteriors, best-fit parameters, and their uncertainties are given in Figure 14. The best-fit Coma cluster GLF is shown in Figure 12 as a solid blue line with its 1σ uncertainty visualized with a shaded blue area. Furthermore, we show the best-fit total GLF in the Coma field consisting of $\Phi_{\rm C}$ and $\Phi_{\rm BG}$ as a turquoise dashed line. We find that $\Phi_{\rm C}$ derived using the maximum likelihood estimate from unbinned data also matches well the completeness and contamination corrected binned data points, as well as $\Phi_{\rm C} + \Phi_{\rm BG}$ matches the completeness corrected binned data points.

We find a significant increase of the GLF slope at $M \gtrsim -18\,g'$ mag, which requires a double Schechter fit and can not be fitted well with a single Schechter function.

We find a fairly steep faint-end slope $\alpha_2 = -1.539^{+0.024}_{-0.024}$. For comparison, Negri et al. (2022) report for massive clusters in the Cluster-EAGLE simulation a significantly flatter faint-end slope in the g band with $\alpha = -1.32 \pm 0.01$.

4.2. Comparison with Other Works on the Coma Cluster GLF

In Figure 15 we compare our derived Coma cluster GLF to previous GLF measurements in the Coma cluster. Direct comparisons of different surveys are problematic, as the shape of the GLF depends on the observed filter band (Beijersbergen et al. 2002), but also on the survey region, e.g., the galaxy number density in the cluster center is inherently higher than in the outer region. We designed our survey to cover a large region ($\approx 1.5 \, \mathrm{deg^2}$) around the Coma cluster center and measured the structural parameters of all galaxies spanning the range from the BCG to dwarf galaxies ($-24.5 \, g' \, \mathrm{mag} \lessapprox M \lessapprox -11.3 \, g' \, \mathrm{mag}$) and containing

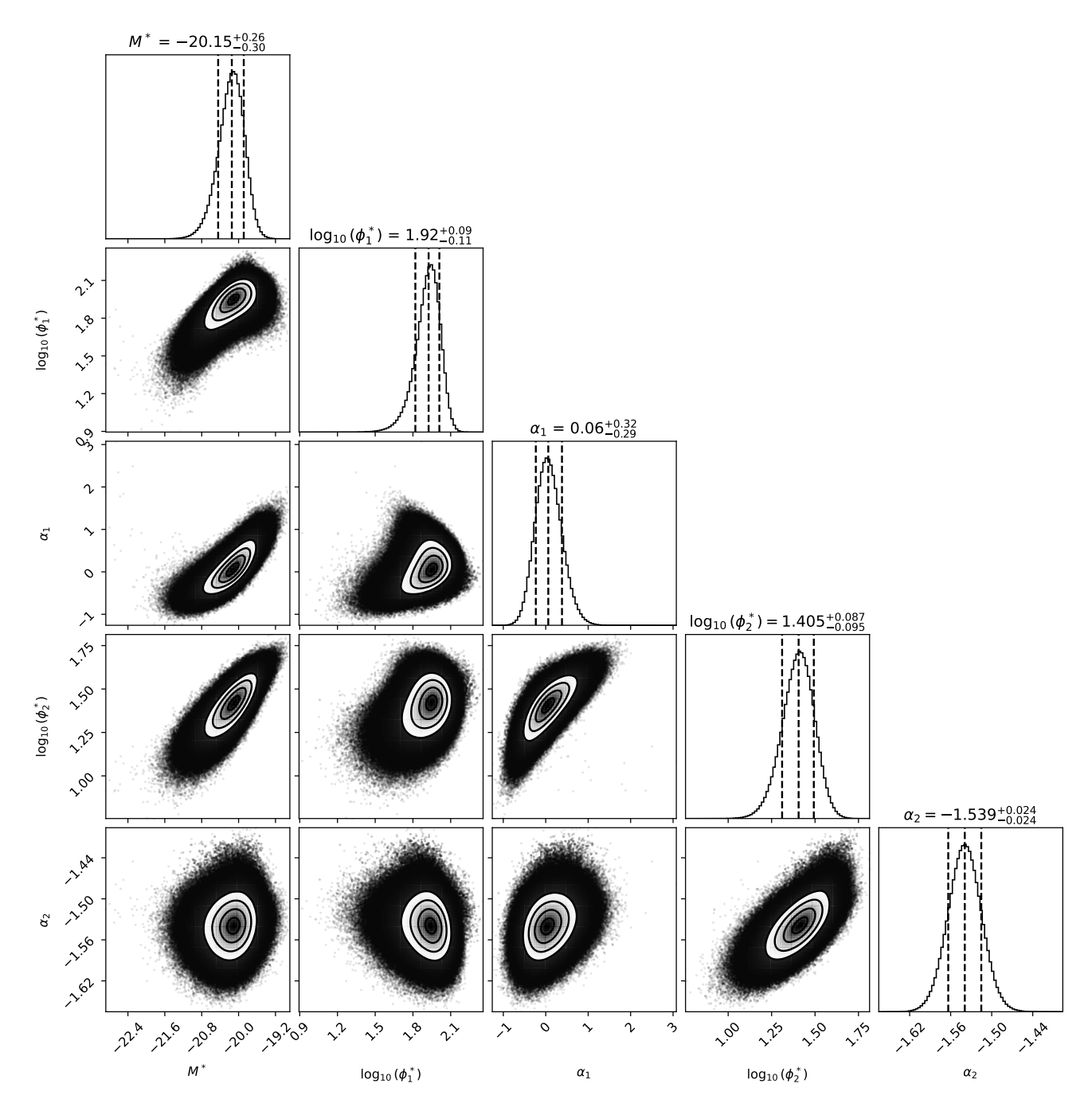


Figure 14. Posterior distribution of the fit of a GLF using a double Schechter function excluding NGC 4889, NGC 4874, and NGC 4839. The contours correspond to the 0.5σ , 1σ , 2σ , and 3σ levels.

a large variety of dwarf galaxies from compact dwarf galaxies to UDGs (Zöller et al. in prep.). This allows us to derive a representative GLF that also probes the faint end well.

As most of the literature GLFs were derived using the R band, we stick for consistency between the literature datasets to their R band GLFs. To convert these measurements to the g' band, we use $r \approx r'$ and g = g' + 0.09

(Willmer 2018) and follow the relation from Jester et al.

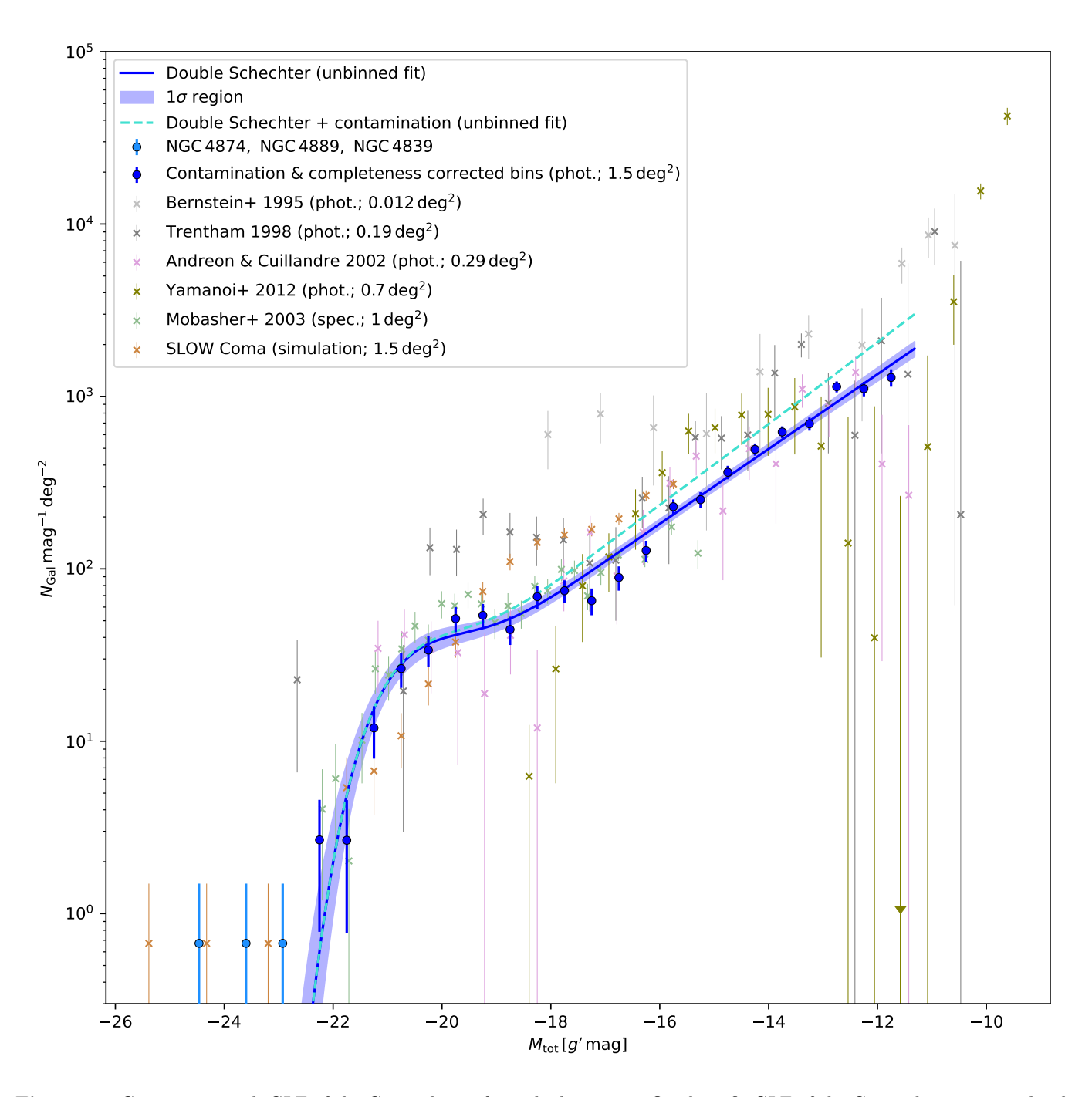


Figure 15. Comparison with GLF of the Coma cluster from the literature. Our best-fit GLF of the Coma cluster is visualized as a blue solid line with its 1σ uncertainty interval in shaded blue. The completeness and contamination corrected bin counts representing the galaxies used for the unbinned GLF fitting procedure are shown in blue, and the three brightest galaxies, NGC 4889, NGC 4874, and NGC 4839, which were not included for the fit, are shown in light blue. The observed GLF from Bernstein et al. (1995) is shown in light grey, those from Trentham (1998) in dark grey, those from Andreon & Cuillandre (2002) in pink, those from Yamanoi et al. (2012) in olive, and those from Mobasher et al. (2003) in light green. Note that one data point from Yamanoi et al. (2012) is outside their plotting range and was therefore not extracted from us. We indicate this point with an arrow marking its maximum possible value. The simulated GLF from the Coma cluster SLOW simulation (Seidel et al. in prep.) is shown in brown. The data points of the three brightest cluster galaxies from our sample and from the SLOW simulation are not binned but shown at their actual positions.

(2005):

$$M_r = M_R + 0.1837(g - r) + 0.0971 \tag{14}$$

$$M_r = M_R + 0.1837(g - r) + 0.0971$$
 (15)

$$+(g-r)-(M_g-M_r)$$
 (16)

$$M_q = M_R + 1.1837(g - r) + 0.0971$$
 (17)

$$M_{g'} = M_R + 1.1837(g' - r') + 0.1136$$
 (18)

Given the red sequence of the Coma cluster (Equation 6) and distance modulus $(m_{g'} - M_{g'} = 35.03)$, we approximate the conversion from the R band to the g' band as:

$$M_{g'} = M_R + 1.1837(-0.023m_{g'} + 1.03) + 0.1136$$
 (19)

$$M_{g'} = M_R - 0.02722(m_{g'} - M_{g'} + M_{g'}) + 1.3328 (20)$$

$$M_{g'} \approx 0.974 \times M_R + 0.369$$
 (21)

We stress here that the comparison with the literature should be considered with caution, especially keeping in mind that the GLF can vary from filter to filter and from field to field (Beijersbergen et al. 2002).

The Mobasher et al. (2003) sample (light green) consists of spectroscopically confirmed galaxies, providing a clean and reliable dataset, though limited to relatively bright galaxies. Their survey covers $1 \deg^2$ around the cluster center, and is hence relatively comparable to our survey region. Their bright-end GLF agrees relatively well with our measurement, showing only slightly higher number densities in the range of $-21.5 g' \text{ mag} \lesssim M \lesssim$ -19 g' mag, which can be explained by their smaller survey area and the fact that their sample is spectroscopically selected and hence contains also blue-cloud and green-valley galaxies, whereas our GLF is only designed to probe the GLF of quiescent red sequence galaxies. This concordance indicates the goodness of our sample selection. However, they report a significantly shallower faint-end slope of $\alpha = -1.18^{+0.04}_{-0.02}$, as they only probe the GLF down to $\approx -15 \, g' \, \text{mag}$. The Trentham (1998) sample (dark grey) has also measured the Coma GLF ranging from bright galaxies to dwarf galaxies but focused only on a small region $(0.19 \, \text{deg}^2)$ in the cluster center. At the bright end, our measurement deviates significantly, but at the faint end, their data points and our best-fit GLF match reasonably well within their uncertainties. However, they find a significantly steeper faint-end slope with $\alpha = -1.7$. The bright-end deviation might be due to them observing only the cluster center and hence finding a higher number density. Similarly, Bernstein et al. (1995) (light grey) analyzed a very small region $(0.012 \, \text{deg}^2)$ in the cluster center, reporting higher number densities. They find a slightly shallower slope of $\alpha = -1.42 \pm 0.05$. Yamanoi et al. (2012) observed very deep data (olive) reaching $\approx -10 \,\mathrm{R\,mag}$.

They are missing the bright end of the GLF as they masked the bright galaxies. At the faint end, they observed a strong decrease in the GLF, followed by a steep increase in their last four data points. Their uncertainties in the range where their GLF strongly decreases are large, but they find the same trend for three different fields. Also Andreon & Cuillandre (2002) report a decrease of the GLF in their last two bins, however, again with large uncertainties. Our faint end of the GLF overlaps with the range where their GLFs are dropping. We do not find any decrease of the GLF in this regime, neither in the best-fit GLF nor in the individual bins that have a significantly smaller uncertainty than their measurements. We conclude that there is no decline of the GLF and no evidence of two distinct dwarf galaxy components in the GLF as suggested by Yamanoi et al. (2012), but that the GLF is steadily increasing. Yamanoi et al. (2012) interpreted their strong increase at the faint end as the contribution by unresolved galaxies and partly by globular clusters. We do not include unresolved objects in our catalog but focus on resolved galaxies. Hence, we can not find this upturn by design of our sample but also due to our magnitude limit. Generally, Bernstein et al. (1995), Trentham (1998), and Yamanoi et al. (2012) focused on small regions but reached fainter magnitudes than our sample, but at the cost of not getting a large and representative sample, which also leads to larger uncertainties than in our survey. Furthermore, we restricted our GLF measurement to a clean sample with good Sérsic fits and accurate u' - g' and g' - r' colors to also derive structural parameter number densities (Zöller et al. in prep.). This restrictive selection limits the completeness at the very faint end but yields a high-confidence measurement of the structural parameters and colors of galaxies, extending to the faintest galaxies used to determine the GLF. The resulting incompleteness is automatically taken into account by the completeness function (see Section 3.6).

Our derived g' band GLF function of quenched red sequence galaxies in the Coma cluster is based on the largest covered area $(1.5 \, \mathrm{deg^2})$ of all datasets, and ranges from the BCG to faint dwarf galaxies ($M \lesssim -11.3 \, g'$ mag), providing a high-precision measurement of the GLF through an unbinned double Schechter fit which is also reflected in the small uncertainties of the binned data points across the entire probed luminosity range. With this, we hope to provide a new benchmark for numerical simulations. Considering the discussion above, we emphasize that for a proper comparison of our GLF with other observations or simulations, an applesto-apples comparison is crucial. The chosen filter band is important, as the color conversion between different

filters is not just a constant offset. The typical g'-r'color is not independent of M, but the red sequence inherits a slope (Equation 6), i.e., fainter galaxies are more blue. This affects the faint-end slope and, assuming a steadily increasing GLF, increases the faint-end slope in the observed magnitude range in the q' band compared to the r' band. Furthermore, choosing a comparable region is especially crucial, as the number density in the center of a galaxy cluster is inherently larger than in the outskirts. Moreover, the GLF in simulations is usually given per volume, for example, in a sphere within the virial radius (Negri et al. 2022), which is physically meaningful, but not directly comparable to most observations that are usually given per area, as determining the distance with the necessary precision for the distance cut is not possible from photometric data. Also, current deep surveys of galaxy clusters in the local universe, such as Coma or Virgo, do not probe the GLF out to the virial radius due to the large spatial extent. For a direct comparison of simulations and observations, the GLF of the simulations has to be restricted to the survey area of an observation and contain all galaxies along the line of sight.

4.3. Comparison with the Coma Cluster Counterpart in the SLOW Simulations

As a direct reference for our results from numerical simulations, we employ a set of constrained zoom-in simulations (LOcal WEb Resimulations with Dynamical friction and Extended blaCK hole Spin model, Seidel et al. (in prep.); Sorce et al. (2015); Sorce (2018)) obtained from the SLOW constrained simulations of the Local Universe (Dolag et al. 2023; Hernández-Martínez et al. 2024). These zoom-in simulations use a modernized version of the Magneticum model (Dolag et al. 2025; Steinborn et al. 2015), adding spin-coupled AGN feedback (Sala et al. 2023; Sala 2024) and an improved prescription for dynamical friction (Damiano et al. 2024). The high resolution zoom-in region $(m_* = 2.6 \times 10^6 M_{\odot})$ used in this work is constructed from a stable Lagrangian region (Seidel et al. 2024) around the wellconstrained Coma¹ counterpart in the SLOW simulation. We place a mock observer at the optimized observer position from Dolag et al. (2023) and select an identical FOV size in order to mimic the observation as closely as possible. To ensure completeness for the simulated GLF, we adapt a lower magnitude cutoff of M = -15.5 g' mag that is set slightly above the stellar

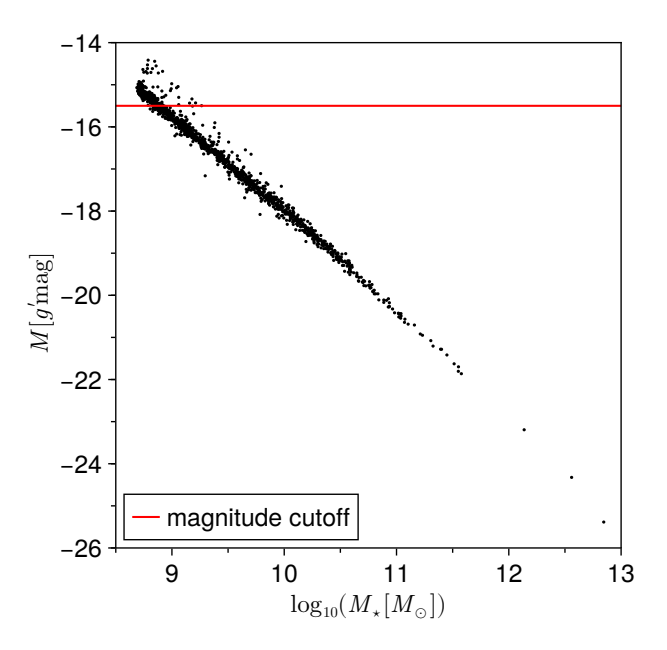


Figure 16. $M_* - M$ scaling for the simulated Coma cluster. The magnitude cutoff at M = -15.5 g' mag is highlighted by the red horizontal line.

mass cut of $5 \times 10^8 M_{\odot}$ we applied due to the mass resolution of the simulation. This can be seen in Figure 16. The resulting GLF is represented by the brown crosses in Figure 15, with the error bars given by the Poisson noise in each bin. Overall, there is good agreement between the simulated and observed GLF, with deviations in the BCG luminosities at the high-luminosity end and an overabundance of simulated galaxies in the intermediate to low-luminosity range compared to the real Coma cluster. We expect the largest uncertainty factor in the simulated luminosity function to be the subgrid model, which can suffer from overcooling. Especially at the low-mass (or respectively low-luminosity) end, insufficient stellar feedback at early times can lead to an overprediction of the stellar mass function in the mass regime where it is expected to be the dominant quenching mechanism (Dolag et al. 2025). The bright-end deficiency relative to the observation, on the other hand, can most likely be explained by the relatively strong AGN feedback, which in turn transfers brighter galaxies to the local peak at around -18 g' mag. Additionally, slight deviations with regard to the dynamical state and assembly history of the Coma counterpart due to uncertainties in the constraints might impact the simulated GLF. We would expect the high-luminosity end to be most sensitive to these large-scale effects, as the mass (and stellar mass) in the BCG and ICL in the cluster can be shown to directly trace its assembly history (Kimmig et al. 2025). Furthermore, we fit a single Schechter function to the

¹ For an alternative re-simulation of the Coma cluster see Malavasi et al. (2023), based on the same constraints, Nr. 8 from the CLONES set (Sorce et al. 2015).

unbinned data points from the SLOW Coma counterpart down to $M<-15\,g'$ mag using the same procedure as outlined before for the actual Coma cluster, also excluding the three brightest cluster galaxies, but without the need for completeness and contamination correction. We find best-fit parameters of $M^*=-20.50^{+0.21}_{-0.24}$, $\log_{10}(\Phi^*)=1.83^{+0.10}_{-0.10},~\alpha=-1.37^{+0.04}_{-0.04}$. The simulated faint-end slope is significantly shallower than our observed one, but the simulation generally predicts a larger number density of dwarf galaxies. This highlights the importance of conducting actual apples-to-apples comparisons to allow for a comparison of the normalization $\log_{10}(\Phi^*)$ and not just α , as comparing the slope alone can lead to a misleading interpretation of the number of dwarf galaxies.

5. SUMMARY AND CONCLUSION

We have obtained deep u'-, g'-, and r' band data for the Coma cluster using the 2.1 m Fraunhofer Wendelstein Telescope with the final survey region covering $1.5\,\mathrm{deg^2}$ and two reference fields with comparable depth and resolution. The Coma cluster data reaches median 3σ surface brightness limits in $10'' \times 10''$ boxes of $(30.0\,\mathrm{u'},\ 29.6\,\mathrm{g'},\ 28.7\,\mathrm{r'})$ mag arcsec⁻².

We have created isophote models and measured the structural parameters, u' - g', and g' - r' colors of the three brightest cluster galaxies NGC 4889 (including the ICL), NGC 4874, and NGC 4839 using isopy. We subtracted these models from the images to allow an accurate measurement of the fainter galaxies. The parameters of the other 403 bright galaxies with $m \leq 18 g'$ mag were also measured using isophotal fitting. Again, we subtracted these models to allow for a reliable detection and measurement of the structural parameters of dwarf galaxies even in the vicinity of those bright galaxies. Furthermore, we presented a method to fully automatically create masks and to measure the structural parameters using GALFIT of more than 10⁵ galaxies in the Coma cluster field. Additionally, we obtained u'-q' and g'-r' of those galaxies using elliptical apertures. Afterward, we selected cluster members based on their quiescent sequence membership in the u'-g' vs g'-r' colorcolor diagram and their red sequence membership and restricted our sample to galaxies with high-confidence measurements of their structural parameters. In total, our final Coma cluster sample comprises 5161 cluster member candidates.

Furthermore, we identically analyzed the two reference fields to quantify the contamination of our Coma cluster sample. Moreover, we have performed injection-recovery tests for the Coma cluster and the reference fields to derive the completeness functions of our sample

selection. For both reference fields, we fitted a Schechter function using the unbinned data points employing the dynamic nested sampling package DYNESTY for an analytical description of the contamination, taking into account the completeness function of the respective reference field, also propagating the uncertainties and probing the uncertainty due to cosmic variance.

Finally, we derived the g' band GLF of the Coma cluster using the unbinned data points of quiescent red sequence galaxies down to $M \approx -11.3 \, q' \, \text{mag}$, excluding the three brightest cluster galaxies. For this, we fitted a double Schechter function using DYNESTY, taking into account the completeness function and the background contamination, and propagated their uncertainties, including the effect of the cosmic variance. We derived the best-fit double Schechter parameters of $M^* =$ $\begin{array}{llll} -20.15^{+0.26}_{-0.30}, & \log_{10}(\Phi_1^*) = 1.92^{+0.09}_{-0.11}, & \alpha_1 = 0.06^{+0.32}_{-0.29}, \\ \log_{10}(\Phi_2^*) = 1.405^{+0.087}_{-0.095}, & \text{and} & \alpha_2 = -1.539^{+0.024}_{-0.024}. & \text{The} \end{array}$ steep faint-end slope in our study is partially driven by the inclusion of low-surface-brightness galaxies, such as UDGs, but especially by a substantial population of compact dwarf galaxies, which is discussed in detail in a complementary analysis of galaxy structural parameter relations by Zöller et al. (in prep.).

This work combines deep wide-field imaging with careful cluster member selection and galaxy profile fitting, along with corrections for incompleteness and contamination, to improve constraints on the Coma cluster GLF. With the resulting GLF we hope to provide a new reference measurement for future observational and theoretical studies of galaxy clusters. The high precision of our approach is also reflected in the small uncertainties of the binned GLF data points across the full luminosity range. The faint-end slope is steeper than predicted by simulations of massive galaxy clusters, such as the Cluster-EAGLE simulation (Negri et al. 2022) with $\alpha = -1.32 \pm 0.01$ for massive galaxy clusters or the Coma cluster counterpart in the SLOW simulation (Seidel et al. in prep.) with $\alpha = -1.37 \pm 0.04$. A steep faint-end slope as $\alpha_2 = -1.539^{+0.024}_{-0.024}$ is more in line with a cold dark matter model than with warm dark matter models, which predict shallower faint-end slopes than cold dark matter models. However, comparing our results to those of most other studies is not straightforward due to the differences in the probed regions and the filters used. Hence, drawing direct conclusions about the nature of dark matter is not yet possible. Also, not only the faint-end slope α_2 should be considered, but also the normalization $\log_{10}(\Phi_2^*)$ to consider the total amount of dwarf galaxies and not just the increase of galaxy number densities with fainter magnitudes. Disentangling the effects of baryonic physics – and their implementation in simulations – from those of dark matter models will remain a central challenge for future studies. Despite these challenges, we attempted to provide a robust benchmark for future simulations to probe baryonic feedback and the nature of dark matter.

6. ACKNOWLEDGEMENTS

The Wendelstein 2.1m telescope project was funded by the Bavarian government and by the German Federal government through a common funding process. Part of the 2.1m instrumentation, including some of the upgrades for the infrastructure, were funded by the Cluster of Excellence "Origin of the Universe" of the German Science Foundation DFG.

This work would not have been practical without extensive use of NASA's Astrophysics Data System Bibliographic Services and the SIMBAD database, operated at CDS, Strasbourg, France.

We also used the image display tool SAOImage DS9, developed by the Smithsonian Astrophysical Observatory, and the image display tool Fitsedit, developed by Johannes Koppenhoefer.

We thank Lucas Valenzuela for providing the CosmoLuminosities julia package for the simulation post-processing.

The authors used OpenAI's ChatGPT and Grammarly to assist with grammar and language polishing of the manuscript. ChatGPT was also used for prototyping parts of the analysis code and for debugging purposes. All code and text generated with these tools were thoroughly reviewed, verified, and adapted by the authors.

Software: Astropy (The Astropy Collaboration et al. 2018), Photutils (Bradley et al. 2020), DYNESTY (Speagle 2020), numpy (van der Walt et al. 2011), scipy (Virtanen et al. 2021), matplotlib (Hunter 2007), SExtractor (Bertin & Arnouts 1996), SCAMP (Bertin 2006), SWarp (Bertin 2010).

REFERENCES

Alam, S., Albareti, F. D., Allende Prieto, C., et al. 2015, ApJS, 219, 12, doi: 10.1088/0067-0049/219/1/12

Andreon, S., & Cuillandre, J. C. 2002, ApJ, 569, 144, doi: 10.1086/339261

Behroozi, P., Wechsler, R. H., Hearin, A. P., & Conroy, C. 2019, MNRAS, 488, 3143, doi: 10.1093/mnras/stz1182

Beijersbergen, M., Hoekstra, H., van Dokkum, P. G., & van der Hulst, T. 2002, MNRAS, 329, 385, doi: 10.1046/j.1365-8711.2002.05004.x

Bennett, C. L., Larson, D., Weiland, J. L., & Hinshaw, G. 2014, ApJ, 794, 135, doi: 10.1088/0004-637X/794/2/135

Bernstein, G. M., Nichol, R. C., Tyson, J. A., Ulmer, M. P., & Wittman, D. 1995, AJ, 110, 1507, doi: 10.1086/117624

Bertin, E. 2006, in Astronomical Society of the Pacific
Conference Series, Vol. 351, Astronomical Data Analysis
Software and Systems XV, ed. C. Gabriel, C. Arviset,
D. Ponz, & S. Enrique, 112

Bertin, E. 2010, SWarp: Resampling and Co-adding FITS Images Together, Astrophysics Source Code Library, record ascl:1010.068

Bertin, E. 2011, in Astronomical Society of the Pacific Conference Series, Vol. 442, Astronomical Data Analysis Software and Systems XX, ed. I. N. Evans,

A. Accomazzi, D. J. Mink, & A. H. Rots, 435

Bertin, E., & Arnouts, S. 1996, A&AS, 117, 393, doi: 10.1051/aas:1996164

Binggeli, B., Sandage, A., & Tammann, G. A. 1985, AJ, 90, 1681, doi: 10.1086/113874 Blanton, M. R., Lupton, R. H., Schlegel, D. J., et al. 2005, ApJ, 631, 208, doi: 10.1086/431416

Bower, R. G., Lucey, J. R., & Ellis, R. S. 1992, MNRAS, 254, 589, doi: 10.1093/mnras/254.4.589

Bradley, L., Sipőcz, B., Robitaille, T., et al. 2020, astropy/photutils: 1.0.0, 1.0.0, Zenodo, doi: 10.5281/zenodo.4044744

Bullock, J. S., & Boylan-Kolchin, M. 2017, ARA&A, 55, 343, doi: 10.1146/annurev-astro-091916-055313

Cash, W. 1979, ApJ, 228, 939, doi: 10.1086/156922

Chilingarian, I. V., & Zolotukhin, I. Y. 2012, MNRAS, 419, 1727, doi: 10.1111/j.1365-2966.2011.19837.x

Cuillandre, J. C., Bolzonella, M., Boselli, A., et al. 2025, A&A, 697, A11, doi: 10.1051/0004-6361/202450808

Damiano, A., Valentini, M., Borgani, S., et al. 2024, A&A, 692, A81, doi: 10.1051/0004-6361/202450021

Dolag, K., Sorce, J. G., Pilipenko, S., et al. 2023, A&A, 677, A169, doi: 10.1051/0004-6361/202346213

Dolag, K., Remus, R.-S., Valenzuela, L. M., et al. 2025, arXiv e-prints, arXiv:2504.01061, doi: 10.48550/arXiv.2504.01061

Dressler, A. 1980, ApJ, 236, 351, doi: 10.1086/157753

Efstathiou, G., Ellis, R. S., & Peterson, B. A. 1988, MNRAS, 232, 431, doi: 10.1093/mnras/232.2.431

Euclid Collaboration, Scaramella, R., Amiaux, J., et al. 2022, A&A, 662, A112,

doi: 10.1051/0004-6361/202141938

- Euclid Collaboration, Mellier, Y., Abdurro'uf, et al. 2025, A&A, 697, A1, doi: 10.1051/0004-6361/202450810
- Faber, S. M., Willmer, C. N. A., Wolf, C., et al. 2007, ApJ, 665, 265, doi: 10.1086/519294
- Ferrarese, L., Côté, P., Sánchez-Janssen, R., et al. 2016, ApJ, 824, 10, doi: 10.3847/0004-637X/824/1/10
- Flewelling, H. A., Magnier, E. A., Chambers, K. C., et al. 2020, ApJS, 251, 7, doi: 10.3847/1538-4365/abb82d
- Gaia Collaboration, Brown, A. G. A., Vallenari, A., et al. 2021, A&A, 649, A1, doi: 10.1051/0004-6361/202039657
- Gómez, P. L., Nichol, R. C., Miller, C. J., et al. 2003, ApJ, 584, 210, doi: 10.1086/345593
- Gössl, C. A., & Riffeser, A. 2002, A&A, 381, 1095, doi: 10.1051/0004-6361:20011522
- Gruen, D., Seitz, S., & Bernstein, G. M. 2014, PASP, 126, 158, doi: 10.1086/675080
- Habas, R., Marleau, F. R., Duc, P.-A., et al. 2020, MNRAS, 491, 1901, doi: 10.1093/mnras/stz3045
- Hernández-Martínez, E., Dolag, K., Seidel, B., et al. 2024, A&A, 687, A253, doi: 10.1051/0004-6361/202449460
- Hopp, U., Bender, R., Grupp, F., et al. 2014, in Society of Photo-Optical Instrumentation Engineers (SPIE)
 Conference Series, Vol. 9145, Ground-based and Airborne Telescopes V, ed. L. M. Stepp, R. Gilmozzi, & H. J. Hall, 91452D, doi: 10.1117/12.2054498
- Hunter, J. D. 2007, CSE, 9, 90, doi: 10.1109/MCSE.2007.55
 Ivezić, Ž., Kahn, S. M., Tyson, J. A., et al. 2019, ApJ, 873, 111, doi: 10.3847/1538-4357/ab042c
- Jester, S., Schneider, D. P., Richards, G. T., et al. 2005, AJ, 130, 873, doi: 10.1086/432466
- Kauffmann, G., White, S. D. M., & Guiderdoni, B. 1993, MNRAS, 264, 201, doi: 10.1093/mnras/264.1.201
- Kimmig, L. C., Brough, S., Dolag, K., et al. 2025, Astronomy & Astrophysics, 700, A95, doi: 10.1051/0004-6361/202554777
- Kluge, M. 2020, PhD thesis, Ludwig-Maximilians University of Munich, Germany
- Kluge, M., & Bender, R. 2023, ApJS, 267, 41, doi: 10.3847/1538-4365/ace052
- Kluge, M., Bender, R., Riffeser, A., et al. 2021, ApJS, 252, 27, doi: 10.3847/1538-4365/abcda6
- Kluge, M., Remus, R.-S., Babyk, I. V., Forbes, D. A., & Dolfi, A. 2023, MNRAS, 521, 4852, doi: 10.1093/mnras/stad882
- Kluge, M., Neureiter, B., Riffeser, A., et al. 2020, ApJS, 247, 43, doi: 10.3847/1538-4365/ab733b
- Kluge, M., Comparat, J., Liu, A., et al. 2024, A&A, 688, A210, doi: 10.1051/0004-6361/202349031
- Kluge, M., Hatch, N. A., Montes, M., et al. 2025, A&A, 697, A13, doi: 10.1051/0004-6361/202450772

- Klypin, A., Kravtsov, A. V., Valenzuela, O., & Prada, F. 1999, ApJ, 522, 82, doi: 10.1086/307643
- Kosyra, R., Gössl, C., Hopp, U., et al. 2014, Experimental Astronomy, 38, 213, doi: 10.1007/s10686-014-9414-1
- Kubo, J. M., Stebbins, A., Annis, J., et al. 2007, ApJ, 671, 1466, doi: 10.1086/523101
- Laureijs, R., Amiaux, J., Arduini, S., et al. 2011, arXiv e-prints, arXiv:1110.3193, doi: 10.48550/arXiv.1110.3193
- Lewis, I., Balogh, M., De Propris, R., et al. 2002, MNRAS, 334, 673, doi: 10.1046/j.1365-8711.2002.05558.x
- Lin, Y.-T., Mohr, J. J., & Stanford, S. A. 2004, ApJ, 610, 745, doi: 10.1086/421714
- Malavasi, N., Sorce, J. G., Dolag, K., & Aghanim, N. 2023, A&A, 675, A76, doi: 10.1051/0004-6361/202245777
- Marleau, F. R., Habas, R., Poulain, M., et al. 2021, A&A, 654, A105, doi: 10.1051/0004-6361/202141432
- Marleau, F. R., Cuillandre, J. C., Cantiello, M., et al. 2025a, A&A, 697, A12, doi: 10.1051/0004-6361/202450799
- Marleau, F. R., Habas, R., Carollo, D., et al. 2025b, arXiv e-prints, arXiv:2503.15335, doi: 10.48550/arXiv.2503.15335
- Mateo, M. L. 1998, ARA&A, 36, 435,
- doi: 10.1146/annurev.astro.36.1.435
- Menci, N., Fiore, F., & Lamastra, A. 2012, MNRAS, 421, 2384, doi: 10.1111/j.1365-2966.2012.20470.x
- Mobasher, B., Colless, M., Carter, D., et al. 2003, ApJ, 587, 605, doi: 10.1086/368305
- Moore, B., Ghigna, S., Governato, F., et al. 1999, ApJL, 524, L19, doi: 10.1086/312287
- Moster, B. P., Naab, T., & White, S. D. M. 2013, MNRAS, 428, 3121, doi: 10.1093/mnras/sts261
- —. 2018, MNRAS, 477, 1822, doi: 10.1093/mnras/sty655
- Moster, B. P., Somerville, R. S., Maulbetsch, C., et al. 2010, ApJ, 710, 903, doi: 10.1088/0004-637X/710/2/903
- Müller, O., Jerjen, H., & Binggeli, B. 2017, A&A, 597, A7, doi: 10.1051/0004-6361/201628921
- Negri, A., Dalla Vecchia, C., Aguerri, J. A. L., & Bahé, Y. 2022, MNRAS, 515, 2121, doi: 10.1093/mnras/stac1481
- Peng, C. Y., Ho, L. C., Impey, C. D., & Rix, H.-W. 2010, AJ, 139, 2097, doi: 10.1088/0004-6256/139/6/2097
- Pillepich, A., Springel, V., Nelson, D., et al. 2018, MNRAS, 473, 4077, doi: 10.1093/mnras/stx2656
- Queirolo, G., Seitz, S., Riffeser, A., et al. 2025, MNRAS, 542, 170, doi: 10.1093/mnras/staf1186
- Román, J., Trujillo, I., & Montes, M. 2020, A&A, 644, A42, doi: 10.1051/0004-6361/201936111

- Sala, L. 2024, Supermassive black hole spin evolution in cosmological simulations,
 - Ludwig-Maximilians-Universität München.
 - http://nbn-resolving.de/urn:nbn:de:bvb:19-341219
- Sala, L., Valentini, M., Biffi, V., & Dolag, K. 2023, Supermassive black hole spin evolution in cosmological simulations with OpenGadget3.
 - https://arxiv.org/abs/2312.07657
- Schechter, P. 1976, ApJ, 203, 297, doi: 10.1086/154079
- Schlafly, E. F., & Finkbeiner, D. P. 2011, ApJ, 737, 103, doi: 10.1088/0004-637X/737/2/103
- Seidel, B. A., Dolag, K., Remus, R. S., et al. 2024, arXiv e-prints, arXiv:2412.08708,
 - doi: 10.48550/arXiv.2412.08708
- Seidel, B. A., Dolag, K., & Sorce, J. in prep.
- Sorce, J. G. 2018, MNRAS, 478, 5199, doi: 10.1093/mnras/sty1631
- Sorce, J. G., Gottlöber, S., Yepes, G., et al. 2015, MNRAS, 455, 2078, doi: 10.1093/mnras/stv2407
- Speagle, J. S. 2020, MNRAS, 493, 3132, doi: 10.1093/mnras/staa278
- Steinborn, L. K., Dolag, K., Hirschmann, M., Prieto, M. A., & Remus, R.-S. 2015, MNRAS, 448, 1504, doi: 10.1093/mnras/stv072
- Struble, M. F., & Rood, H. J. 1999, ApJS, 125, 35, doi: 10.1086/313274
- Sérsic, J. L. 1968, Atlas de Galaxias Australes
- The Astropy Collaboration, Price-Whelan, A. M., Sipőcz, B. M., et al. 2018, The Astronomical Journal, 156, 123, doi: 10.3847/1538-3881/aabc4f
- Trentham, N. 1998, MNRAS, 293, 71, doi: 10.1046/j.1365-8711.1998.01125.x

- van der Walt, S., Colbert, S. C., & Varoquaux, G. 2011, CSE, 13, 22, doi: 10.1109/MCSE.2011.37
- van Dokkum, P. G., Abraham, R., Merritt, A., et al. 2015, ApJL, 798, L45, doi: 10.1088/2041-8205/798/2/L45
- Venhola, A., Peletier, R., Laurikainen, E., et al. 2017, A&A, 608, A142, doi: 10.1051/0004-6361/201730696
- —. 2019, A&A, 625, A143,doi: 10.1051/0004-6361/201935231
- Virtanen, P., Gommers, R., Burovski, E., et al. 2021, scipy/scipy: SciPy 1.6.3, v1.6.3, Zenodo, doi: 10.5281/zenodo.4718897
- Visvanathan, N., & Sandage, A. 1977, ApJ, 216, 214, doi: 10.1086/155464
- Williams, R. J., Quadri, R. F., Franx, M., van Dokkum, P., & Labbé, I. 2009, ApJ, 691, 1879, doi: 10.1088/0004-637X/691/2/1879
- Willmer, C. N. A. 2018, The Astrophysical Journal Supplement Series, 236, 47, doi: 10.3847/1538-4365/aabfdf
- Wittmann, C., Lisker, T., Ambachew Tilahun, L., et al. 2017, MNRAS, 470, 1512, doi: 10.1093/mnras/stx1229
- Wright, A. H., Robotham, A. S. G., Driver, S. P., et al. 2017, MNRAS, 470, 283, doi: 10.1093/mnras/stx1149
- Wright, E. L. 2006, PASP, 118, 1711, doi: 10.1086/510102
- Yagi, M., Koda, J., Komiyama, Y., & Yamanoi, H. 2016, ApJS, 225, 11, doi: 10.3847/0067-0049/225/1/11
- Yamanoi, H., Komiyama, Y., Yagi, M., et al. 2012, AJ, 144, 40, doi: 10.1088/0004-6256/144/2/40
- York, D. G., Adelman, J., Anderson, Jr., J. E., et al. 2000, AJ, 120, 1579, doi: 10.1086/301513
- Zöller, R., Kluge, M., & Bender, R. in prep.
- Zöller, R., Kluge, M., Staiger, B., & Bender, R. 2024, ApJS, 271, 52, doi: 10.3847/1538-4365/ad2775